Interfacial characteristics and cohesion mechanisms of linear friction welded dissimilar titanium alloys: Ti–5Al–2Sn–2Zr–4Mo–4Cr (Ti17) and Ti–6Al–2Sn–4Zr–2Mo (Ti6242)

Xavier Boyat, Dorick Ballat-Durand, Julie Marteau, Salima Bouvier, Jérôme Favergeon, Andrey Orekhov, Dominique Schryvers

Interfacial characteristics and cohesion mechanisms of linear friction welded dissimilar titanium alloys: Ti-5Al-2Sn-2Zr-4Mo-4Cr (Ti17) and Ti-6Al-2Sn-4Zr-2Mo (Ti6242)

Xavier Boyat[a], Dorick Ballat-Durand[a], Julie Marteau[a], Salima Bouvier[a], Jérôme Favergeon[a], Andrey Orekhov[b], Dominique Schryvers[b]

[a]Alliance Sorbonne Universités, Université de Technologie de Compiègne, Laboratoire Roberval de Mécanique FRE UTC-CNRS 2012, Centre de Recherche Royallieu - CS 60 319 - 60 203 Compiègne Cedex, France

[b] EMAT, Department of Physics, University of Antwerp, Groenenborgerlaan 171, BE-2020, Antwerp, Belgium

Corresponding author: julie.marteau@utc.fr

ABSTRACT

A detailed microstructural examination endeavoring to understand the interfacial phenomena yielding to cohesion in solid-state assembling processes was performed. This study focuses on the transition zone of a dissimilar titanium alloy joint obtained by Linear Friction Welding (LFW) the β-metastable Ti17 to the near-α Ti6242. The transition zone delimitating both alloys is characterized by a sharp microstructure change from acicular HCP (Hexagonal Close-Packed) α' martensitic laths in the Ti6242 to equiaxed BCC β (Body-Centered Cubic) subgrains in the Ti17; these α' plates were shown to precipitate within prior-β subgrains remarkably more rotated than the ones formed in the Ti17. Both α' and β microstructures were found to be intermingled within transitional subgrains demarcating a limited gradient from one chemical composition to the other. These peculiar interfacial grains revealed that the cohesive mechanisms between the rubbing surfaces occurred in the single-phase β domain under severe strain and high-temperature conditions. During the hot deformation process, the mutual migration of the crystalline interfaces from one material to another assisted by a continuous dynamic recrystallization process was identified as the main adhesive mechanism at the junction zone. The latter led to successful cohesion between the rubbing surfaces. Once the reciprocating motion stopped, fast cooling caused both materials to experience either a $\beta_{lean} \rightarrow \alpha'$ or $\beta_{lean} \rightarrow \beta_{metastable}$ transformation in the interfacial zone depending on their local chemical composition. The limited process time and the

subsequent hindered chemical homogenization at the transition zone led to retaining the so-called intermingled α'/β_m subgrains constituting the border between both Ti-alloys.

Keywords

Friction welding, microstructure, titanium alloy, grain boundary migration, interface joining mechanism, solid-state joining.

1 INTRODUCTION

The mechanisms leading to cohesion in solid-state assembling processes of mutually soluble metallic alloys are observed, studied and applied with success in various industrial joining techniques. An intuitive assumption states that bringing together metal atoms from the faying in-contact surfaces within the range of interatomic distance would result in the formation of a metallic bond by mutual sharing of non-localized electrons. Yet, the oxide films or extraneous adsorbed species which interfere as a physical barrier to the material coalescence must inevitably be preliminary disrupted or decomposed [1]. In forge and large deformation based assembling processes such as accumulative roll bonding or in various forms of pressure welding techniques, the asperities between the faying surfaces are collapsed by means of important plastic deformation, while the contaminants are breakdown by the local strain in the joining zone [2], [3], [4]. In diffusion bonding processes, macroscopic deformations are avoided and the bond formation is mainly obtained by the material transport phenomena taking place across the materials being joined. The applied pressure and the high-temperature conditions facilitate local contaminant break-up and dispersion at the contact points. However, the thermal dissolution of oxides and surface contaminants was demonstrated as a significant thermo-chemical mechanism to achieve the bond formation [5]–[8]. Besides, the physical mechanisms induced by local plastic creep deformation, such as grain sliding and restoration/recrystallization mechanisms, were also outlined in the literature as key phenomena favoring cohesion in diffusion assembling techniques [9], [10] .

Linear Friction Welding (LFW) is a solid-state assembling process in-between these categories. Indeed, the LFW process combines the features of frictional heating in dry tribological contacts [11] with the ones of plastic-deformation induced assembling processes and solid-state diffusion bonding techniques. In linear friction welding, the weld is obtained by pressing a work-piece (forging part) into another one that describes a linear reciprocating motion (oscillating part). The control of the friction process is ensured through three independent parameters as: the contact pressure, the oscillating amplitude and the frequency. With adapted process parameters, the local heat generation by friction at the interface and the consequent thermal softening cause the materials to plastically flow and lead to the coalescence of the rubbing parts into a thin metallurgical bond.

The ability to assemble dissimilar alloys is one of the most promising applications of LFW technology. Indeed, the latter is of high technological interest for replacing mechanical assemblies and to produce innovative multi-material and multi-functional parts. In addition, this class of processes is also highly appreciated in the aircraft industry for producing/repairing blade-disk assemblies as well as to obtain near-net-shape parts. Recent studies involving the successful assembling of dissimilar titanium alloys [12]–[16] demonstrated viable configurations which exhibited satisfying mechanical strengths for practical applications. Assembling Ti-alloys can be done using dissimilar microstructures or different grades. Detailed descriptions of the central weld zone are often given but without identifying the phenomena at the origin of the bonds between materials. As an example, Guo *et al.* [14] gave a detailed description of the microstructure of a LFW joint between Ti-6Al-4V and Ti-6Al-2Sn-4Zr-6Mo and thoroughly characterized the texture of the central weld zone. However, they did not clarify the interfacial mechanisms responsible for solid state bonding. The underlying mechanisms leading to the bond formation in friction assembling processes and, more broadly, on mutually soluble solid-state assembling processes are still debated in the literature [17], [18]. Hence, in an attempt to clear up the interfacial mechanisms responsible for solid-state bonding, extensive observations and chemical analyses were performed in the close vicinity of the transitional zone of such a joint.

The present work endeavors to clarify the operating phenomena contributing to the bond formation at a microstructural scale between two dissimilar, but mutually soluble, Ti-alloys: the β-metastable Ti-5Al-2Sn-2Zr-4Mo-4Cr (Ti17) and the near-α Ti-6Al-2Sn-4Zr-2Mo (Ti6242). These alloys were chosen because of their strong differences in microstructures formed under rapid cooling from the Solution-Treated (ST) configurations: acicular HCP (Hexagonal Close Packed) α' martensitic laths in the Ti6242 and BCC (Body-Centered Cubic) $\beta_{metastable}$ equiaxed grains in the Ti17. The former will help to identify the welding interfacial zone as it will lead to a sharp α'/ β_m phase contrast.

2 MATERIALS & METHODS

A butt-welding test campaign was carried out using the commercial standard titanium alloy grades: Ti-6Al-2Sn-4Cr-2Mo and the Ti-5Al-2Sn-2Zr-4Mo-4Cr. Pairs of solid blocks of 15 x 80 x 70 mm^3 were cut by electrical-discharge machining from 250 mm diameter and 570 mm length standard forged billets of (TIMETAL®6-2-4-2 or commonly denominated Ti6242) and (TIMETAL®17, Ti17) provided by TIMET Savoie S.A., France. The extracted specimens were linear friction welded in an open-air environment on the 15 x 80 mm^2 surface with the 80 mm edge parallel to the oscillation direction $\langle x \rangle$ as depicted in Figure 1. It is also noted that the 80 mm edge is parallel with the billet axis.

Prior to the welding procedure, the raw assembling surfaces were polished with P120 SiC grinding paper. The Ti6242 block was used as the oscillating part whereas the Ti17 block was used as the forging part. The machine used to obtain the linear friction weld is an MDS-30 developed by the ACB Company, Nantes, France. The process parameters selected in this study were: a forging pressure of 90 MPa, a frequency of 50 Hz and a 2 mm amplitude. The process lasted about 3 s using a 5 mm axial shortening; a forging pressure of 90 MPa was maintained for a duration of 10 s after the end of the oscillating motion.

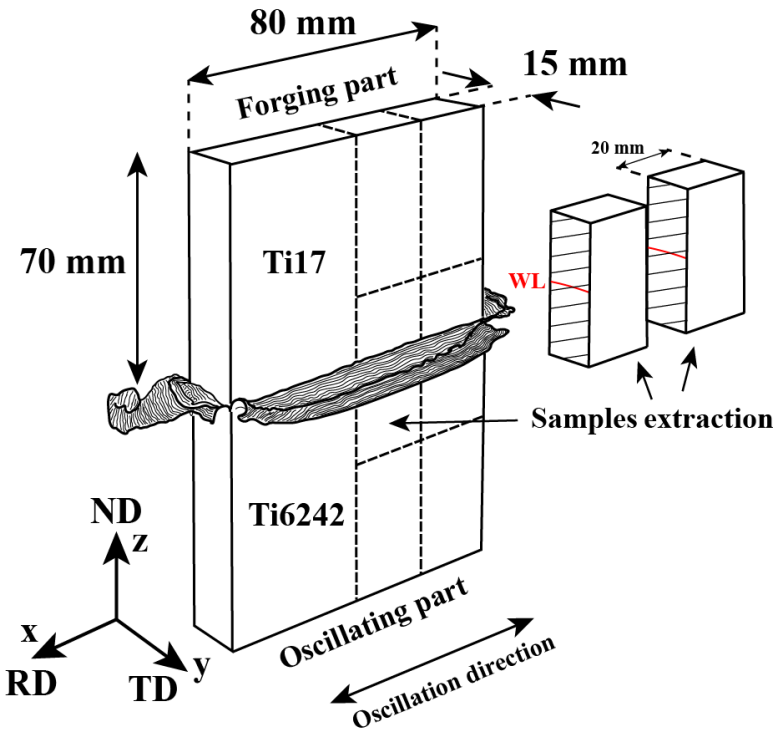

Figure 1: Schematic illustration of a Ti17 – Ti6242 linear friction weld assembly and the sampling strategy.

Both the Ti17 and the Ti6242 are conventional Ti-alloys widely used in the aircraft industry for structural parts or intermediate-temperature compressor disks respectively. The materials were provided in the solution treated then aged configuration (STA). The Ti6242 used in this study is characterized by an initial microstructure consisting mainly of coarse α nodules presenting an ellipsoid shape with interspersed residual intergranular β matrix. On another note, the Ti17 exhibited an as-received Widmanstätten α+β microstructure formed by the intragranular precipitation of fine entangled hardening α laths within large prior-β grains. Their respective β-transus temperatures specified by the manufacturer are of approximately: 995°C for the Ti6242 and 890°C for the Ti17. Both microstructures are presented in Figure 2.

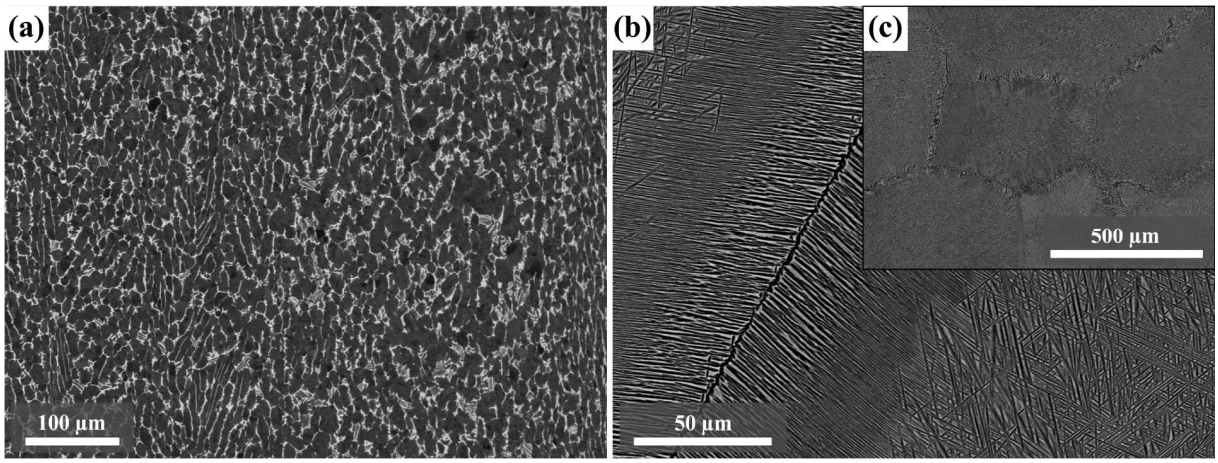

Figure 2: (a) SE-SEM image of the Ti6242 base material, (b)-(c) SE-SEM image of the Ti17 base material.

The microstructural characterization of the transition zone of the dissimilar joint was carried out on representative samples collected from cross-sectional cuts in the welded work-pieces, orthogonal to the friction direction of the welding process. A schematic representation of the extraction procedure is illustrated in Figure 1. The microstructural observations were then carried out on the (Y, Z) plane of the extracted samples, close to the central section of the weld joint. For surface preparation, the specimens were mechanically polished through standard abrasive polishing procedures using SiC abrasive grinding papers (P80, P220, P1200, P2400 and finally P4000 grit sizes). The final grinding procedures were performed using successive polishing with standard diamond solutions down to 1 µm mean diameter on a polyester cloth. Finishing was done using a 40% oxide polishing suspension (OPS) solution and 60% in volume of H_2O on a Buehler VibroMet™ 2 vibratory polisher.

Microstructural observations were performed using a tungsten Field Emission Gun Zeiss Σigma Scanning Electron Microscope (FEG-SEM). The Electron Back-Scattered Diffraction (EBSD) mapping was obtained using a Nordiff OptiPlex 7040 detector for Kikuchi pattern image capture. The specimens were mounted onto a 70° tilted holder and a 20 mm working distance was used. The measurement steps were chosen according to the resolution required for the analyses. The orientation

maps were then calculated using the TSL OIM data collection™ software and the EBSD post-processing procedures were finally performed on the Matlab© open-source toolbox Mtex [19], [20] v5.1.1. The high-current beam voltage was equal to 15 kV for imaging and to 25 kV for EBSD mapping. The sample reference used to formulate the EBSD orientation data is defined with the "rolling direction" RD parallel with the friction direction $\langle x \rangle$. The "normal direction" ND is parallel with the forge direction $\langle z \rangle$ and the "transverse direction" TD is orthogonal to the (RD, ND) plane and corresponds to the $\langle y \rangle$ direction (Figure 1). Clean-up procedures were applied on the EBSD orientation cartographies: before grain detection, a first correction was applied on the isolated non-indexed pixels with a median filter procedure taking into account the orientations of the adjacent neighboring pixels. Besides, the pixels with a confidence index lower than 0.1 were deleted from the analyses.

The atomic force microscopy (AFM) imaging was done using a Bruker acquisition system in tapping mode. The metallographic sample for AFM imaging was mechanically polished then chemically etched with a Struers-A3 electrolytic solution at 6 °C.

For Transmission Electron Microscopy (TEM), 1 mm thick slices of cross-sectioned weld samples were cut in the (X, Z) plane using a micro-cutting machine. The slices were then contoured down to 3 mm diameter disc-shaped foils. Afterward, the extracted thin foils were mechanically pre-thinned to reach a 100 µm thickness. The resulting slices were finally polished using a conventional twin-jet polishing technique at 20 V and -30°C with a solution of 10% (in vol.) perchloric acid diluted in a 20% 2-butoxyethanol. TEM observations were carried out with a FEI Tecnai OSIRIS S/TEM equipped with the Super-X SDD EDX detector and a second FEI Tecnai F20 TEM combined with the NanoMegas ASTAR system for automated phase/orientation mapping of nanocrystals materials. Both microscopes were operated at an accelerating voltage of 200kV. For orientation data acquisition, the condenser aperture was equal to 30 µm, the spot size was 8 nm and the scan step size was equal to 5 nm.

3 RESULTS

3.1 Overview of the microstructural changes

The microstructure of the dissimilar LFW joint was preliminary observed by SEM in Back-Scattered Electron (BSE) mode, the corresponding micrographs are presented in Figure 3. The Welding Line (WL) is easily identifiable due to the glaring differences in microstructural features (i.e. morphologies, phases) with both Ti6242 and Ti17 former starting microstructures (i.e. fully-equiaxed and Widmanstätten respectively). Indeed, a significant microstructure refinement can be noted in this zone that exhibits a remarkable fragmentation of the β matrix phase accompanied, in the Ti6242, by the intragranular precipitation of discernible acicular α' martensitic laths (Figure 3.b-c). Neighboring the fully-transformed WL, an apparent Thermo-Mechanically Affected Zone (TMAZ) was revealed in the form of gradually plasticized grains and dissolved morphologies (i.e. smeared former β matrix in the Ti6242 and α precipitates dissolution in the Ti17). Seemingly unaffected microstructures were recovered at approximately 1 mm and 2.5 mm in the Ti6242 and Ti17 respectively.

In complement to imaging, orientation data measurements were carried out by EBSD technique to further investigate the microstructural changes across the joint. The resulting HCP and BCC orientation maps superimposed with the calculated grain boundaries are shown in Figure 4. Yet, since the crystal structures of α phase and α' martensitic phase (space group $P6_3/mmc$) are very similar, the EBSD indexing software was unable to distinguish the difference. Consequently, the α' phase would be indexed as α.

Seven main areas showing noteworthy differences in microstructure were identified in Figure 3 and Figure 4 which complement with each other. The different microstructural zone will be subjected to separated analyses. Starting from the WL and going to the left (*i.e.* Ti6242 side), an about 400 µm thick band of HCP indexed microstructure can be observed (Zone III). A detailed examination of the morphologies constituting the local microstructure by SEM imaging in Figure 3.b shows the probable precipitation of acicular α' laths within seemingly refined equiaxed prior-β grains (of 10 µm

mean grain size). No distinct retained β phase was identified within this acicular microstructure. In the near-WL zone of the Ti6242 (i.e. II./III. border in Figure 3 and 4), the corresponding micrographs revealed a gradual distribution of the β stabilizers from the initially interspersed intergranular β_{rich} matrix (i.e. former equilibrium β matrix enriched in β-stabilizing elements) to the adjacent plasticized α nodules resulting in a white cloudy aspect on BSE imaging signal (Figure 3.b). The latter was not present near the WL which might indicate that an extensive chemical composition homogenization occurred in this zone during the frictional process. Thereafter (Zone II in Figure 4.a), a fragmented-like microstructure was observed with a progressive apparition of the initial β matrix as moving further away from the WL. Then, a sharp delimitation can be identified from the fragmented-like α nodules to a seemingly unaffected microstructure (Zone I).

Now, starting from the WL and going to the right side (i.e. Ti17), Zone IV is characterized by a 200 µm thick band of refined equiaxed β grains (10 µm mean grain size). Then, one can notice the presence of squashed large β grains on an about 1 mm thick band (zone V) originating from the starting Widmanstätten microstructure of the base material. These grains exhibit an elongated aspect in the direction of the material expulsion directions (i.e. RD & TD) and noteworthy intragranular misorientation gradients. The apparent grain refinement in the zone V is preferentially located in the vicinity of the coarse β grains boundaries forming necklace structures [17]; this phenomenon is more pronounced near Zone IV. Further on, just plasticized β grains are observed in zone VI. Then in zone VII, the starting Widmanstätten α+β mixture is progressively recovered, first with the presence of α Grain-Boundary layers (α_{GB}) followed by the α intragranular laths (α_{WI}).

In addition to that, a remarkable texture development is present in both the Ti17 and the Ti6242 indicating a significant crystal reorientation to the deformation conditions during the process. This reorientation appeared to be rather limited to the WL in the Ti17 but extended to 700 µm from the weld center line in the Ti6242; in the latter, both, the α fragments and the retained β matrix, were subjected to this reorientation. In order to visually highlight the local crystal preferred orientation development within the weld, the IPF color code has been chosen to represent the crystallographic

direction of the indexed lattice along the RD direction (friction direction) on the orientation maps depicted in Figure 4 and Figure 12 (which corresponds to the normal direction of these maps). Similar microstructure morphologies, phase presence, and texture were reported in Ballat-Durand *et al.* [21] and [22] for single-material joints using analogous LFW conditions.

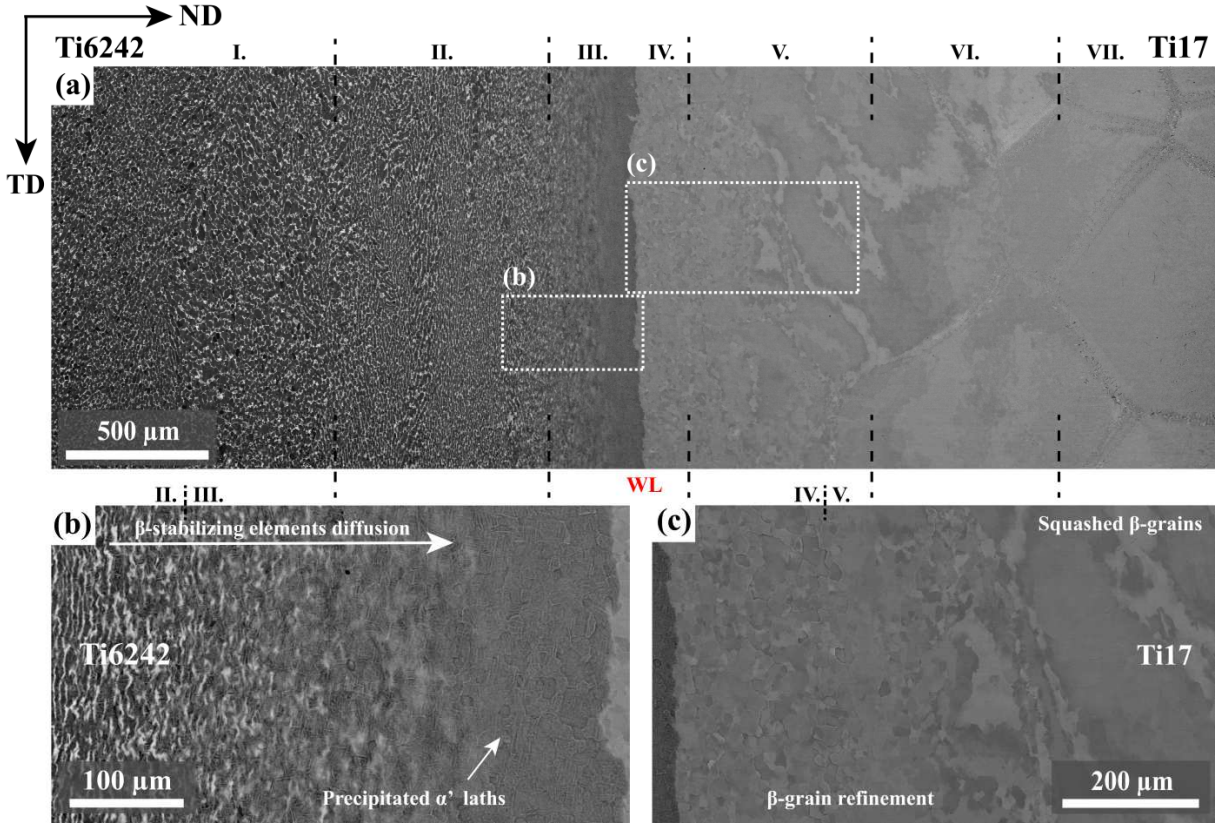

Figure 3: BSE-SEM micrographs of the dissimilar Ti6242/Ti17 LFW joint. (a) Overview of the weld interface; (b) zoom at the Ti6242 TMAZ; (c) zoom at the Ti17 TMAZ.

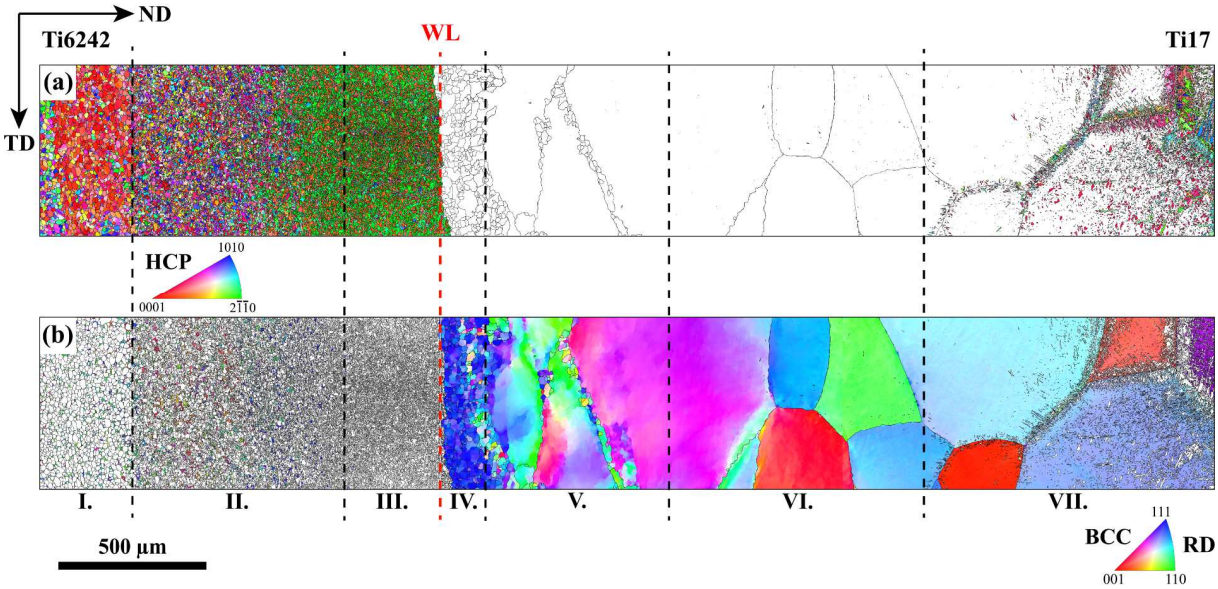

Figure 4: Inverse pole figures obtained from EBSD analysis (0.5 µm step size) of the Ti6242/Ti17 LFW joint showing (a) the HCP and (b) BCC indexed data superimposed with the grain boundaries (5° orientation angle threshold); the colors represent the crystallographic direction of the indexed lattice along RD direction.

3.2 Close microstructural and chemical investigations at the transition zone

The SEM micrographs of the interfacial zone (Figure 5.a and 5.b) revealed a side-by-side coexistence of sharp needle-like α' structures with a β microstructure which offers a stark microstructural contrast from one side to the other. Closer observations of the junction zone showed the presence of round-shaped porosities with diameters that do not exceed 1 µm. In the transition zone, both phases appeared to be intermingled within seemingly common β subgrains. Besides, AFM topographic imaging revealed a close interpenetration of the in-contact microstructures along the transition zone (Figure 5.c). Deeper analyses were therefore performed in SEM and TEM in an attempt to understand the phenomena that could form such a peculiar structure as well as to thoroughly characterize the interfacial zone.

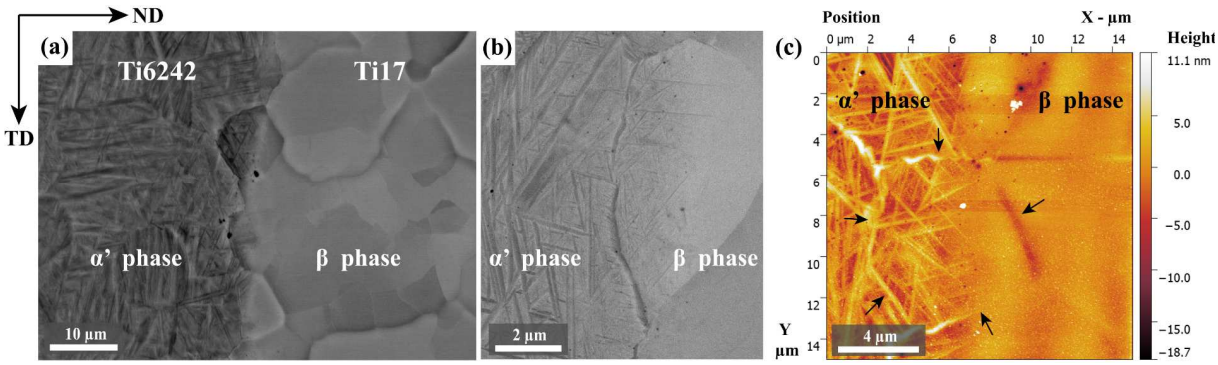

Figure 5: (a), (b) BSE-SEM image of the interfacial zone, (c) AFM tapping mode imaging of the interfacial zone, the black arrows highlight an intermingled interfacial subgrain.

First, the local distribution of substitutional elements across the interfacial zone was investigated through energy-dispersive X-ray spectroscopy in TEM; the corresponding qualitative element cartographies are presented in Figure 6. The gradual signal intensity in the near interfacial zone around the apparent heterophase interface is easily noticeable on the Cr signal (Figure 6.d) due to the absence of the latter among the alloying elements of the Ti6242. A detailed chemical analysis was conducted along with a cross-line profile shown in Figure 7. The resulting interdiffusion profiles across the interface present a typical error-function aspect and an interdiffusion band of approximately 4 µm in thickness is discernable in the transition zone.

A basic one-dimension model was applied from the experimental data (Figure 7) with the aims of roughly estimate the order of magnitude of the interdiffusion phenomenon during the high-temperature processing time. The plateau-like aspect on both sides of the element diffusion profiles seems to corroborate the hypothesis of a local homogeneous partition of the solute elements in the adjacent microstructures on either side of the transition zone. The latter hypothesis was notably speculated after back-scattered electron microscopy observations (Figure 3.b-c). Equation (1) is then the error-function solution of the classic 1D semi-infinite manifolds diffusion model considered; where C is the concentration of an element at a distance equal to x; C1 and C2 are the solute limits in the Ti6242 and the Ti17 alloys respectively. The values of C1 and C2 were determined from the alloys standard composition, considering the homogeneous solute partition assumption formulated above.

The duration (t) was set as the steady-state axial shortening stage which is about 1.3 s. The estimated diffusion coefficients D_{fit} of the different elements were then computed by fitting the following error-function to the measured data. The estimated values of the diffusion coefficient D_{fit} for the substitutional elements in Ti-alloys are listed in Table 1:

$$(1) \quad C(x)=\frac{C_1-C_2}{2}.\mathrm{erf}\left(\frac{x}{2\sqrt{D_{fit}t}}\right)+\frac{C_1+C_2}{2}$$

Table 1 : Estimated diffusion coefficient D_{fit} of the substitutional elements.

Alloying element	**Al**	**Mo**	**Cr**	**Zr**
D_{fit} [$\mu m^2.s^{-1}$]	0.35	0.25	0.41	0.59

The Sn element variation was excluded from the analysis since both alloys contain equivalent quantities in mass proportion. One should also note that the centers of the error-function profiles do not actually correspond with the visible limit of the interface: a slight shift of the fitted curves towards the martensitic side was observed.

Lastly, local substitutional elements repartition cartographies were realized at high magnification in TEM focusing on the close interfacial zone. The results are displayed in Figure 8. Thin pile-ups of Cr and Mo elements are observed in the in-contact β phase around the α'/β heterophase bounds while important depletions of the latter are observed within the precipitated α' laths. A slight but similar trend seems to appear on the Zr signal as well, even though the intensity contrast on the cartography remains unclear. This phenomenon is not clearly discernible on the other elements at such a measurement scale.

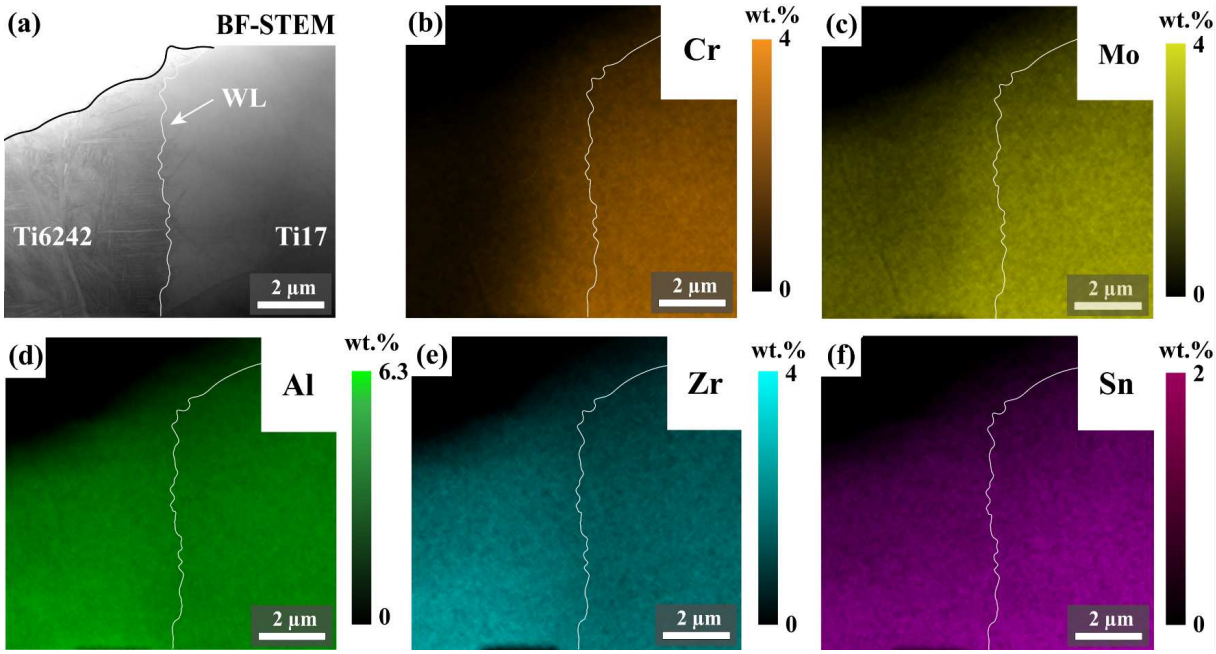

Figure 6: (a) BF-STEM image of an intermingled prior-β subgrain and the corresponding EDX intensity maps of the solute elements: (b) Cr, (c) Mo, (d) Al, (e) Zr, (f) Sn (intensity bar scaled on the wt.%).

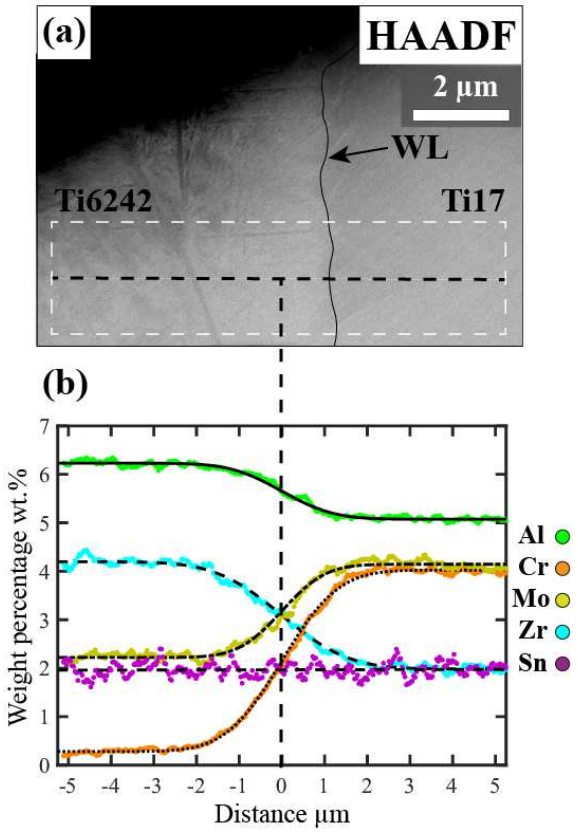

Figure 7: (a) HAADF image of the interfacial zone for EDX profile analysis; (b) line profile of element composition distribution across the Ti6242/Ti17 interface in wt.%.

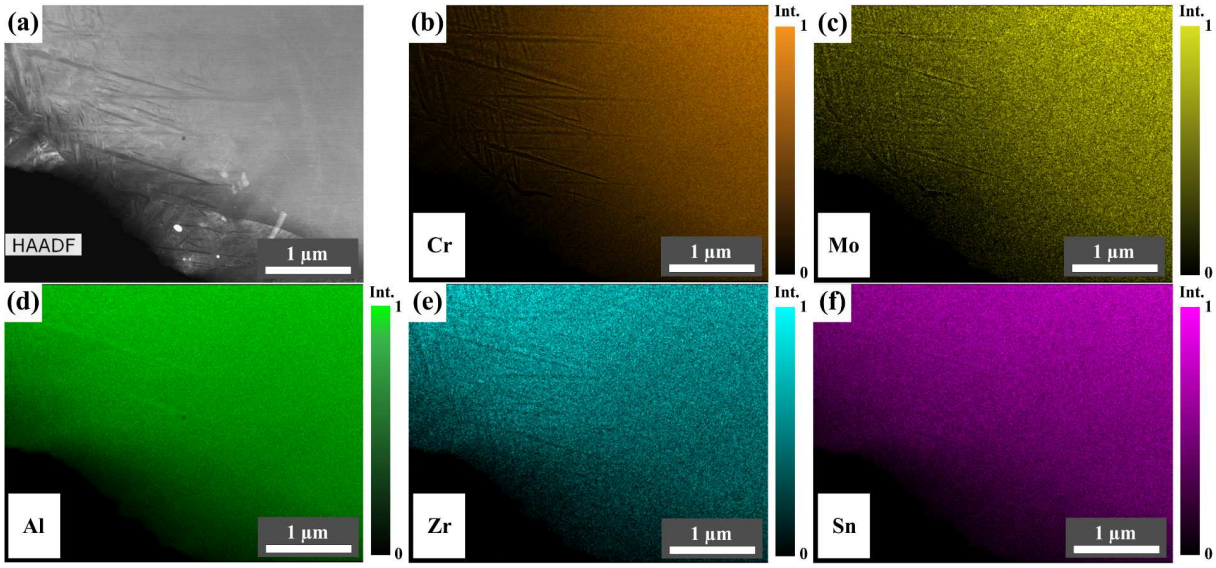

Figure 8: (a) High magnification HAADF image of the close interfacial zone; local EDX intensity maps of the solute elements: (b) Cr, (c) Mo, (d) Al, (e) Zr, (f) Sn.

Additional crystal orientation investigations were carried out in the vicinity of the interfacial zone. The aims for such an approach are twofold: first, to clarify a prospective relationship between the in-contact β-metastable phase and the adjacent precipitated α' phase in the transitional zone and second; to reconstruct the microstructure history from the final state observations considering the thermo-mechanical processing conditions relating to the friction assembling process.

EBSD analyses were first carried out in the vicinity of the interfacial zone. The resulting HCP and BCC inverse pole figures are shown in Figure 9.a and 9.b respectively; superimposed grain boundaries are also provided.

The change in crystallographic structure that operates under external constraints from the high-temperature β-parent lattice to the α' (or α) product crystal structure is known to theoretically follow coordinated rules minimizing the strain energy of phase transformation [23], [24]. Consequently, a self-developed subroutine detailed by authors in [22] using the Matlab toolbox Mtex

v5.1.1 and based on the work of Germain *et al* [25], [26] permitted to reconstruct the parent β orientation prior to the $\beta_{lean} \rightarrow \alpha'$ among clusters of entangled HCP laths relying on the following Burgers Orientation Relationship (BOR) [27]: $\{110\}_{\beta}$ // $\{0001\}_{\alpha'}$ and $\langle 111\rangle_{\beta}$ // $\langle 11\bar{2}0\rangle_{\alpha'}$. The approach may be summarized as it follows: for each precipitated α' needle, the algorithm first computed every possible theoretical β parent orientations using the ideal Burgers orientation relationship (taking into account the 5.268° rotation shift around the $(0001)_{\alpha'}$ zone-axis between β and α' phases). A cross-check comparative procedure was then applied between groups of three neighboring laths surrounding the considered α' needle and separated by high angle grain boundaries (>15° threshold). The β-reconstructed parent grain was then computed as the common BCC orientation solution triplet that minimized the misorientation between the tested laths while respecting a 5° misorientation threshold. This algorithm was then repeated for all the spatial lath combinations of the maps. The reconstructed β orientations are shown in Figure 9.c. and a schematic representation depicting the BOR is provided in Figure 9.e.

The high-temperature β-reconstructed map confirms unequivocally the occurrence of a mutual β-phase intermingling of the materials in the interfacial zone. Closer examinations of the orientation relationship correspondences were then carried out on the interfacial subgrain outlined in red in Figure 9.(a, b, c). In order to clearly illustrate the BOR, the orientations of the map presented in Figure 9 were shifted to align the {110} plane direction of the red-highlighted parent β subgrain with the RD direction corresponding to the out-of-plane normal direction of the map. The stereographic projections of each individual α' lath orientations formed in the Ti6242 side of the selected subgrain were superimposed to the β orientation of the latter (i.e. Ti17 side), the resulting 110-111 and 0001-11$\bar{2}$0 pole figures are shown in Figure 9.d. The red circles on these pole figures indicate that the BOR is actually resolved which confirms the existence of a β microstructural continuity between both alloys during the LFW configuration presently studied. Additional investigations by TEM and the corresponding ASTAR analysis supported as well this statement plus showed that the α' martensitic laths at the juncture between the materials are directly embedded within the β matrix (Figure 10 and

Figure 11). The BOR is systematically shown on the needle-like formations. However, since at the tip of the embedded needles their width as seen in the TEM image is only around 10 nm, the thickness of the sample can be expected to be around 50 nm or higher and no overlapping of diffraction patterns is seen in the central pixels of the needle, these needles should be considered as 2D cross-sections of thin plate structures (Figure 11).

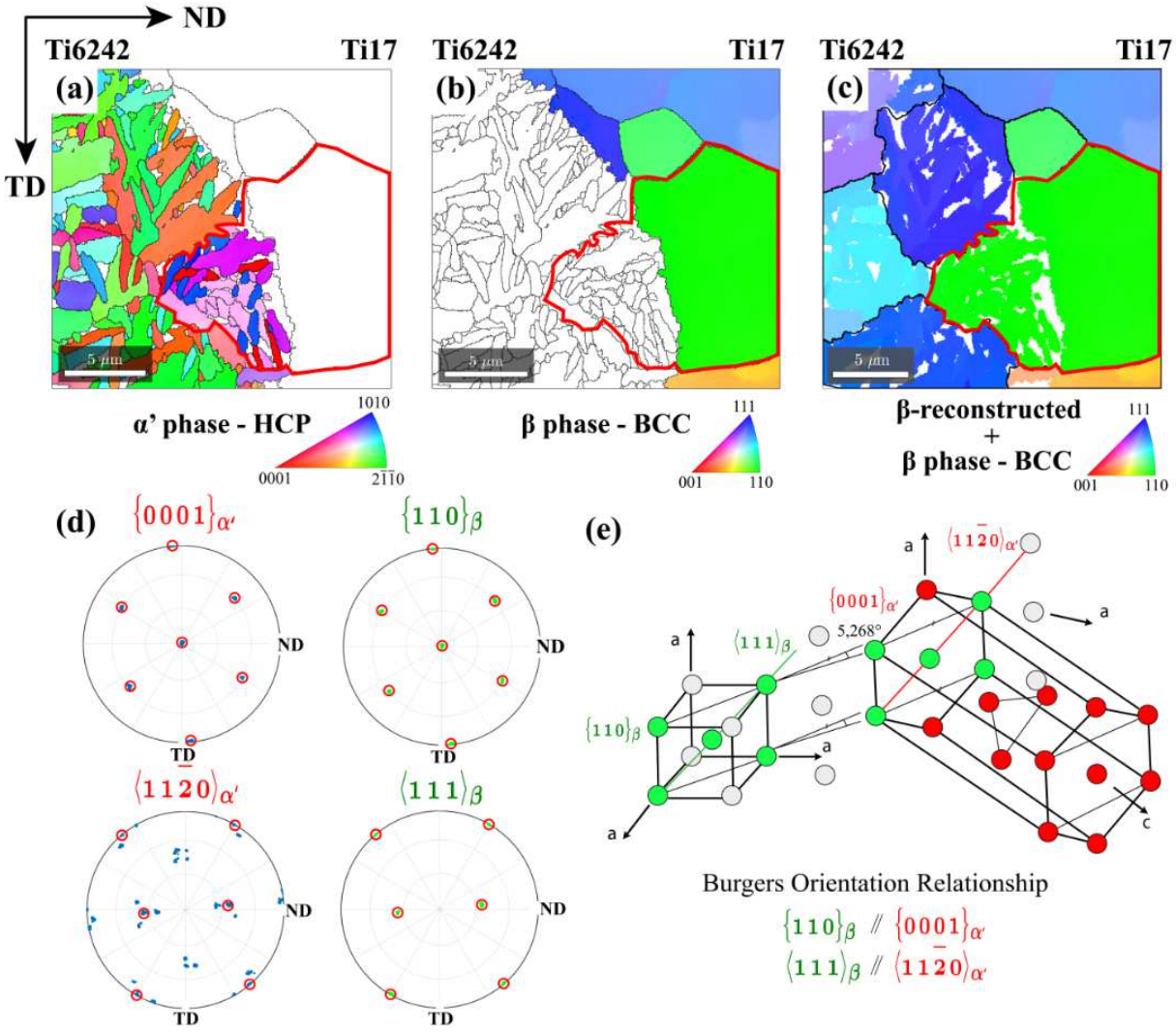

Figure 9: Inverse pole figure from EBSD analysis at the Ti6242/Ti17 transition zone for (a) the HCP, (b) BCC indexed data and (c) the BCC reconstructed orientations; (d) 110-111 and 0001-11$\bar{2}$0 pole figures for, respectively, the HCP and BCC indexed data within the selected subgrain (red boundary); (e) Schematic representation of the Burgers Orientation Relationship; a step size of 40 nm was used

for the EBSD data acquisition and solely the points with a confidence index higher than 0.1 were considered in this analysis; a threshold of 2° misorientation was used for grain boundary detection.

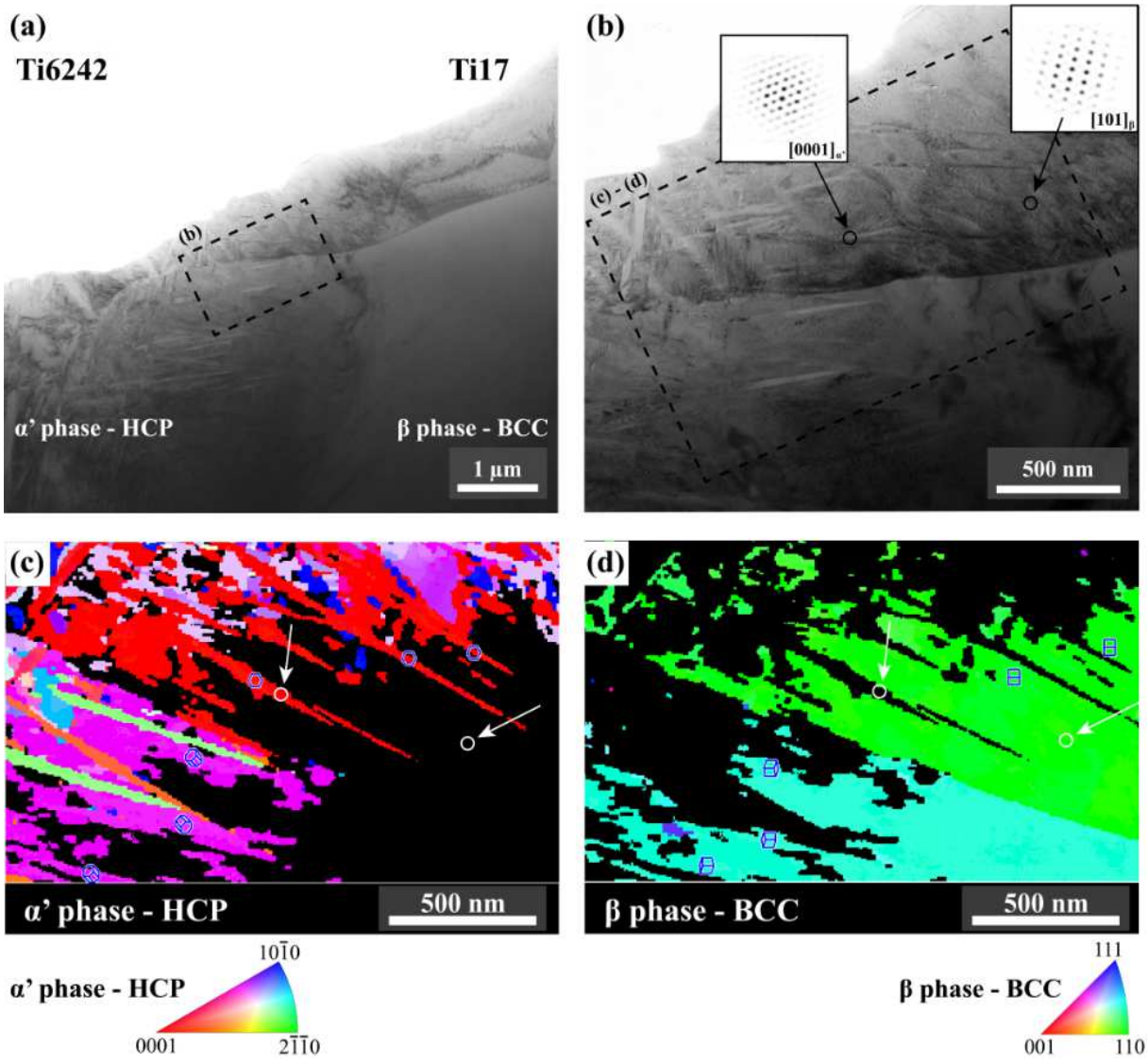

Figure 10: (a) TEM bright field imaging of the interfacial zone along the welding line, (b) High magnification image of the interface combined with diffraction spots obtained in an α' lath and in the β phase; ASTAR inverse pole figure of (c) the HCP and (d) the BCC crystals, the white circles represent the positions of the diffraction spots used in (b).

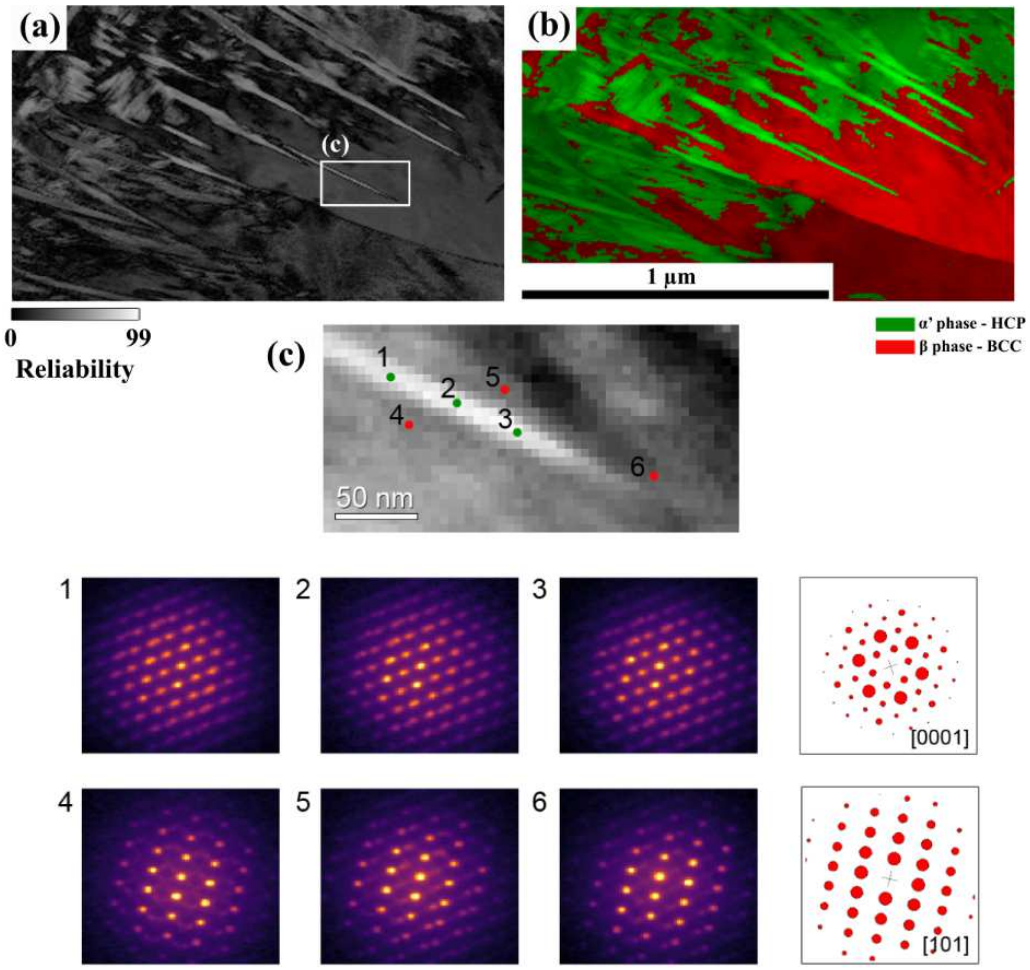

Figure 11: (a) Reliability map of the ASTAR orientation acquisition in TEM, (b) α'-HCP and β-BCC phase map; (c) experimental diffraction patterns obtained on local spots on an α' needle-like formation embedded within β phase matrix comparison with simulated patterns for the [0001] α'and [101] β phase, correspondly.

3.3 Grain fragmentation and texture development

An overview of the near-interfacial zone from EBSD investigations is presented in Figure 12.(a, b, c). A classification of the grain boundary misorientations is also provided combined with a Kernel Average Misorientation (KAM) cartography in Figure 12.d; the KAM procedure was solely applied to the Ti17 side. A fragmented microstructure is discernible in both materials characterized by a remarkably high fraction of low-angle grain boundaries arranged in mosaic patterns. Such a microstructure would indicate that extensive grain fragmentation occurred accompanied by substantial

crystallite rotations. These apparent crystallites constitute substructures with low internal misorientations formed within deformed large β grains. Some local interpenetrations of materials are also readily observable despite the presence of a notable β microstructural continuity revealed in the β-reconstructed configuration.

The distributions of the misorientation angles in the BCC Ti17 (Figure 13.a) and the reconstructed BCC Ti6242 microstructures (Figure 13.b) corroborate the occurrence of a significant grain fragmentation and a subsequent texture development. Indeed in both microstructures, the spatially correlated and uncorrelated misorientation distributions revealed the presence of a noteworthy statistical peak at the low angle boundaries; the former being significantly higher than the latter. Such a feature would indicate that a reorientation of the grains towards a specific direction occurred during LFW accompanied by gradual rotation of the crystallites from low-angle to high-angle grain boundaries. The mechanism forming such textured recrystallized-like microstructures is often referred to as a Continuous Dynamic Recrystallization (CDRX) process [28] and appeared to be more pronounced in the Ti6242 than in the Ti17. In addition, a secondary peak at 60° could be noted in the Ti6242 and is presumably due to the formation of a twin-symmetric texture component. The latter was not as readily visible in the Ti17.

The 111 and 110 pole figure projections of the individual orientations from the EBSD orientation data presented in Figure 12 are plotted in Figure 13.c and 13.d. The stereographic projections were first realized on the (TD, ND) cross-sectional plane, along the friction direction RD and according to the Schmidt equal-area convention. The 111 and 110 pole figure representations highlight the formation of a common two-component β texture development in the near-thermomechanical affected zone of both titanium alloys. A strong crystallites reorientation is notably observed and resulted in the alignment of the BCC <111> crystal direction with the RD. Where the RD also corresponds to the friction direction of the welding process. Furthermore, the texture components manifest a twin-symmetry from one another that is characterized by a 180° rotation around <111>/RD, eventually resulting in a misorientation angle of 60° towards each other. In the

Ti6242, both twin texture components are developed with equivalent observable intensities. While a limited but discernible development of the second twin-symmetric texture component was noted in the Ti17.

Regarding the mechanical load produced by the alternate friction motion, it is interesting to reposition the problem on the longitudinal cross-section of the welded assembly. The latter corresponds to the (RD, ND) plane in the sample reference system. Indeed, the deformation process is ideally comparable with a classic case of simple shear deformation, where the predominant shear deformation would be introduced by the movement of the lower block rubbing against the upper block along the friction direction RD. By analogy, the friction direction would consequently correspond to the shear direction SD, and the shear plane would correspond to the friction plane (RD, TD). Finally, the shear plane normal (SPN) would hence be aligned with the ND. The corresponding 111 and 110 equal-area pole figure projections in the above-defined shear frame reference (SD, SPN) (or also (RD, ND)) are presented in Figure 14.a and 14.b. The ideal shear texture components that may develop in BCC materials were reported in the literature by Baczynski and Jonas [29]. They identified four ideal preferred orientations: D, E, F and J, that develop along two partial fibers: $\{110\}\langle uvw\rangle$ and $\{hkl\}\langle 111\rangle$, during torsion tests realized on α-BCC iron alloys. A schematic representation of these ideal texture components is depicted in Figure 14.c.

The preferred orientation components developing in the near thermo-mechanical affected zone of the weld were then compared with the ideal orientations of the texture components developing in simple shear deformations (Figure 14). The comparative identification analyses consequently exhibited a predominant development of the D1 and D2 twin-symmetric texture components in Ti6242 during the LFW process. In Ti17, only limited development of the D2 component was observed, while a strong crystal preferred reorientation developed towards the D1 component. Both ideal orientations D1 $(\bar{1}\bar{1}2)[111]$ and D2 $(11\bar{2})[111]$ lie on the $\{hkl\}\langle 111\rangle$ fiber and tend to align the $\langle 111\rangle$ crystal direction with the shear/friction direction (SD and RD). As previously remarked, the D1 and D2 component display a 180° rotation symmetry around the shear direction, which also corresponds to the

<111>/RD partial fiber. These findings are consistent with the texture developments observed in the LFW literature on the residual β phase of Ti64 alloy [12], [30] and reported on the texture analyses of a β-metastable alloy [31].

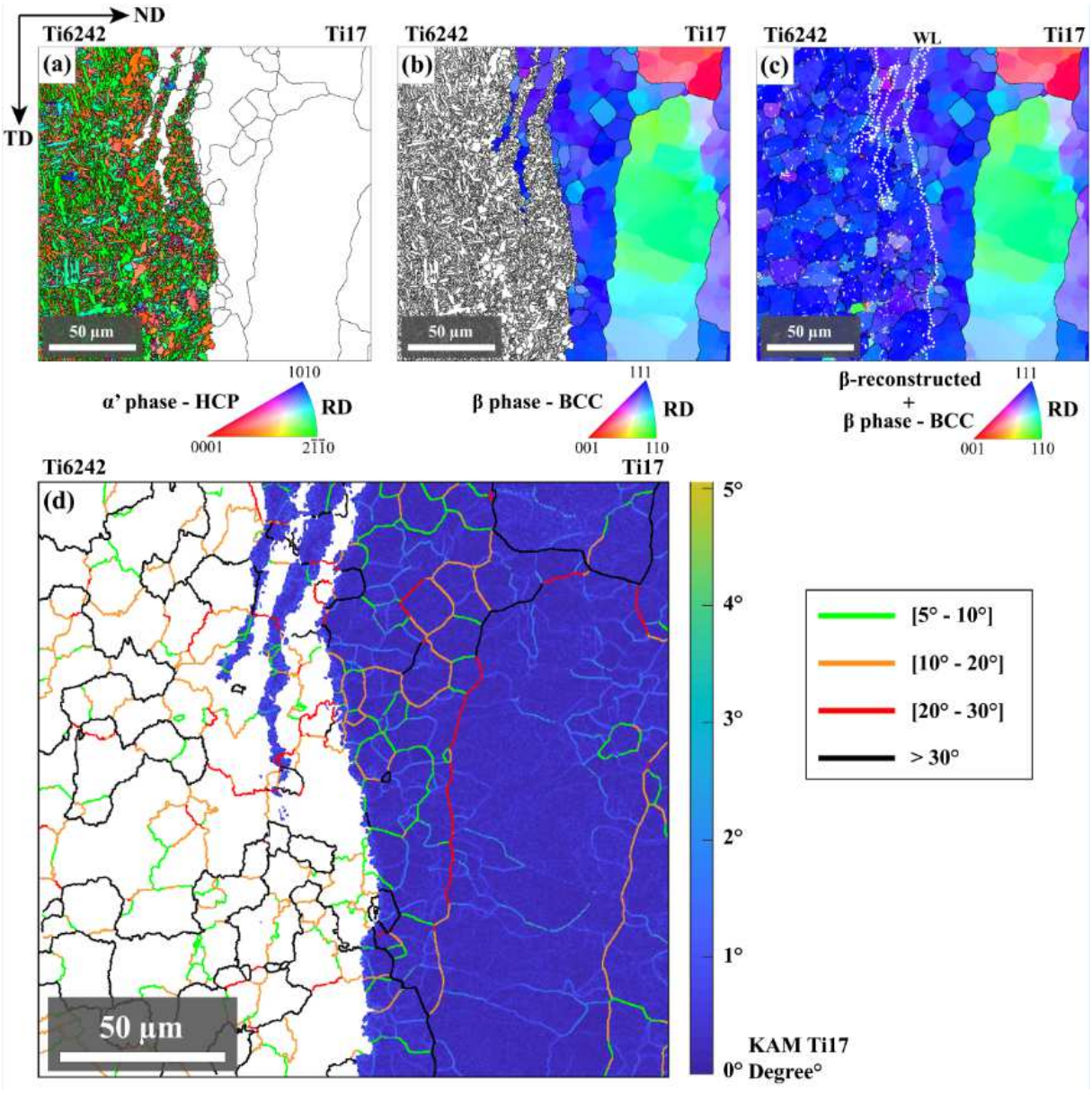

Figure 12: Inverse pole figure from EBSD analysis (step-size 0.2 µm) at the extended Ti6242/Ti17 interfacial zone for (a) the HCP, (b) BCC indexed data and (c) the BCC reconstructed orientations superimposed with the grain boundary detection (5° misorientation threshold); the IPF color code corresponds to crystallographic direction of the indexed lattice along the RD (friction) direction. (d)

The corresponding Kernel Average Misorientation (KAM) cartography combined with the grain boundary misorientation classification.

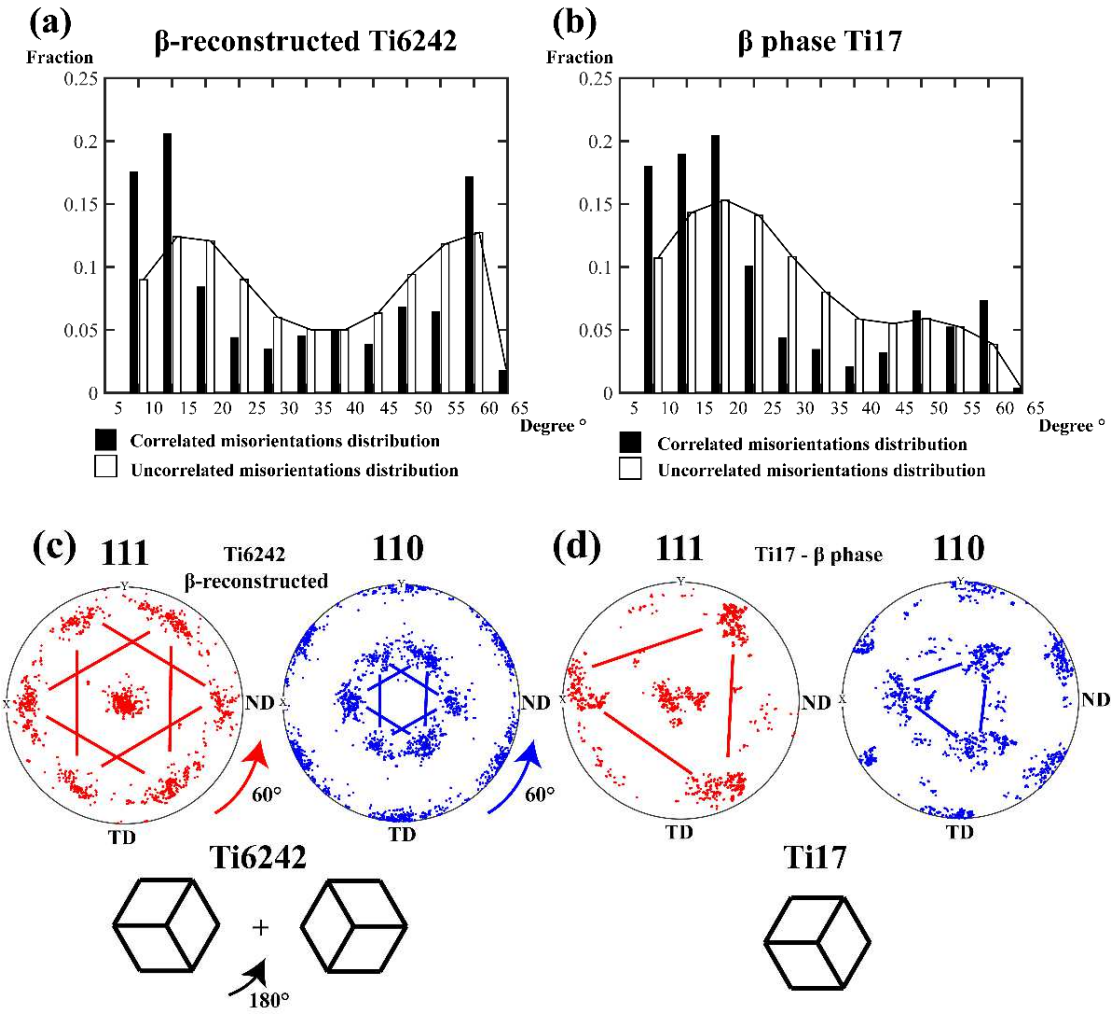

Figure 13: Spatially correlated and spatially uncorrelated misorientation angles distributions for (a) the Ti6242 β-reconstructed and (b) the Ti17 β microstructures; the corresponding 111 and 110 pole figures for (c) the Ti6242 and (d) the Ti17, the equal-area stereographic projections of the orientations are done along the RD (friction) direction in the (TD, ND) plane.

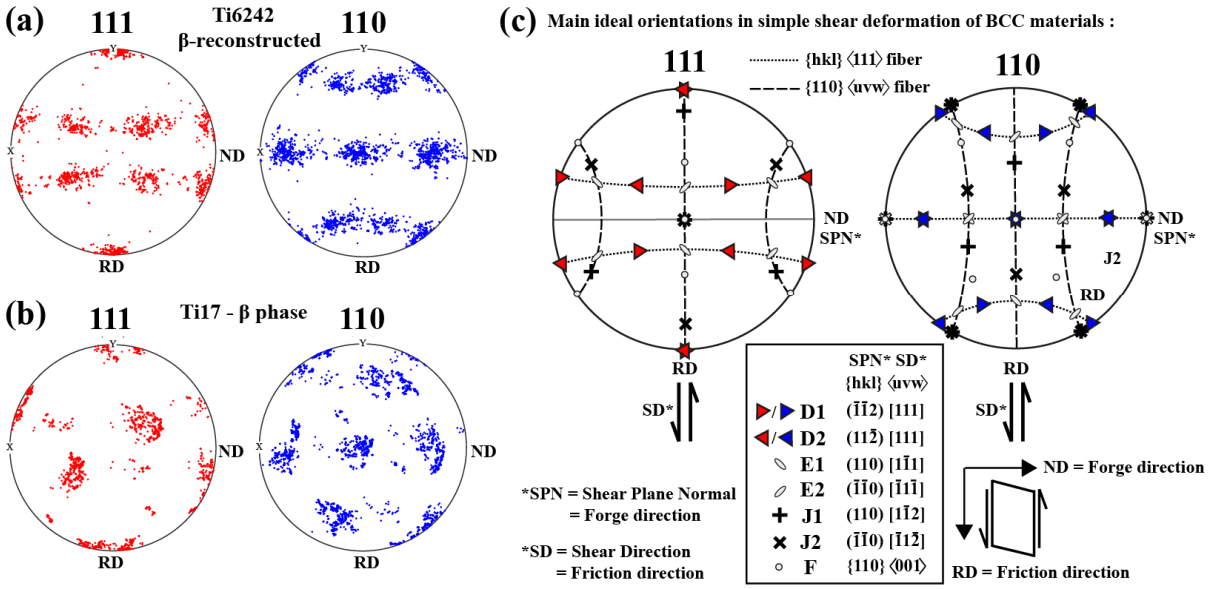

Figure 14: Equal-area 111 and 110 pole figure projections in the (RD, ND) shear frame reference and along the TD for: (a) the Ti6242 β-reconstructed and (b) the Ti17 β phase; the schematic representation of the main ideal orientations in simple shear deformation of BCC materials is illustrated in (c) after [29] and [32] for the ideal shear orientations convention.

4 DISCUSSION

The overviews of the microstructure in the joint (Figure 3 and Figure 4) showed that both Ti17 and Ti6242 alloys present markers of an extensive α→β phase transformation that occurred during the process.

In the Ti6242, these markers are present within a band of approximately 1 mm in thickness (corresponding to the Zones II and III). On the one hand, the former α nodules of the near WL area (Zone III) first underwent a β phase transformation during the hot deformation process. The observed redistribution of the Ti6242 alloying elements was most likely caused by the progressive diffusion of the β stabilizing elements from the initially interspersed intergranular β_{rich} matrix to the adjacent β transformed nodules. The gradual aspect of the diffusion phenomena is directly related to the local temperature distribution which lowers as moving away from the WL. The close WL area rather experienced the highest temperature values. As a result in the latter zone, the rates of the transport phenomena were important enough to lead to substitutional elements partitioning close to a local β_{lean}

composition on a 100 µm thick band of grain refined β microstructure. Where the β_{lean} composition consequently stems from the homogeneous partition of the alloy elements above the β transus. Besides, the alleged extensive chemical homogenization corroborates with the observation of α' martensitic phase in the Zone III. Indeed, the precipitation of the metastable phase α' can only result from the decomposition of a β_{lean} (or quasi-β_{lean}) phase upon rapid cooling to room temperature [33] when the cooling rates are high enough to hinder long-range diffusion phenomena.

On the other hand, in the TMAZ (Zone II) the former α nodules were similarly subjected to above β transus temperatures and consequently underwent β phase transformation as well. However, the limited dwell time in the β domain restrained the diffusion of the β stabilizers from the matrix to the solute lean $\beta_{transformed}$ zones, which resulted in retaining intergranular β matrix upon quenching. The decomposition of these $\beta_{transformed}$ nodules upon cooling led to the precipitation of intertwining α plates (often referred to as $\alpha_{secondary}$) presenting a fragmented-like appearance. The fragmented aspect was attributed by authors in a previous study [22] to a nucleation-shear mechanism leading to the precipitation of various α plates following different crystallographic variants within former $\beta_{transformed}$ parent nodules. This transformation-induced process finally resulting in such fragmented-like α microstructure, with the progressive presence of intergranular β matrix.

In the Ti17, the markers of α→β transformation are present within a 2.5 mm thick band from the WL (Zone IV, V, VI, VII), the cooling rates from the β domain were high enough to result in the stabilization of a single β-metastable phase at room temperature. The afore-mentioned descriptions are in conformity with the ones previously reported by Ballat *et al.* [21], [22] for Ti17 and Ti6242 single-material LFW configurations using the same block geometries and analogous process parameters. Furthermore, Ballat *et al.* [21], [22] also performed *in situ* temperature measurements in the vicinity of the rubbing surfaces and reported that the local interfacial temperature reached about 1200°C. The observed microstructural changes on the Ti17-Ti6242 dissimilar joint are in agreement with these measurements.

To identify the mechanisms resulting in bond formation, the β-grain boundaries of both materials were closely observed in the vicinity of the interfacial junction. In Figure 12.d, the features of β-grain fragmentation and rotation are clearly discernible in both materials with the presence of subgrain structures exhibiting low intragranular misorientation levels. These subgrains subdivide the prior-deformation β-parent grains in smaller crystallites. As illustrated in Figure 5 and, more closely in Figure 9, the interfacial zone exhibits an apparent continuity characterized by the presence of intermingled α'/β grains. The comprehension of the origin of those intermingled grains is a crucial element for the extensive understanding of the creation of bonding.

To this end, the hypothetic parent crystallographic relationship between the α' phase and the β phase has been prospected *via* EBSD and TEM investigations in the junction zone (Figure 9, 10 and 11). A perfect verification of the specific BOR was demonstrated in these peculiar intermingled structures between the precipitated α' laths of the Ti6242 and the corresponding β-metastable structure of the Ti17. Such findings reveal that both structures unequivocally shared the same β-parent crystallographic orientation above β-transus temperature conditions, and indicates that the cohesion mechanisms actually occurred between single-phase β structures.

β titanium is a BCC high stacking fault energy structure, under such hot working conditions, the appearance of a significant dynamic recovery is a characteristic feature [34]–[36]. High-temperature conditions promote the mobility of dislocations and the mutual interaction of their associated elastic fields yield to their self-organization into dislocation wall structures. The result of those complex many-body interactions is the progressive building of new grain boundaries to geometrically accommodate the strain with respect to the mechanical interactions between neighboring grains [37]. In recovery processes, the dislocation generation is balanced by the rate of dislocation annihilation, while a fraction is consumed by the formation of geometrically necessary and incidental boundaries that progressively subdivide the parent grains into smaller crystallites with low dislocation density [35]. Those structures correspond to the reported observations (Figure 12.d) with the

progressive and continuous transformation of the geometrically necessary boundaries into low angle grain boundaries and finally to high angle grain boundaries.

Globally, the Ti17 was shown to exhibit a larger amount of low to medium grain boundaries than the Ti6242. The higher proportion of high angle grain boundaries in the latter observed in Figure 12.d and Figure 13 is probably caused by advanced crystallite rotations and the subsequent development of the two-component D1/D2 simple shear texture (Figure 14). These components are the result of the progressive grain rotation occurring in the near-thermomechanical affected zone in order to tend to the most favorable active slip configuration regarding the imposed plastic flow during the process Indeed, the usual features of crystal plasticity in BCC structures essentially occur by slip on the $\{110\}$, $\{112\}$ and $\{123\}$ planes, which all contain the $\frac{1}{2}\langle 111\rangle$ Burgers vector (dominant slip direction) [38]. As a consequence, during the hot deformation process, the continuous lattice rotation favored the alignment of the $\langle 111\rangle$ BCC primary slip direction with the shear/friction direction. The dominant alignment of the $\{112\}$ slip planes with the friction plane finally led to the observed D1/D2 twin-texture development. It was notably noted that the D1 component development was greatly favored in the Ti17 part. One possible explanation for the asymmetric fragmentation-rotation behavior between Ti6242 and Ti17 may be due to the smaller β grains ($D \approx 20\ \mu m$) forming in the TMAZ of the Ti6242 compared to ones present in the Ti17 side (millimetric). Indeed, smaller grains imply higher density of grain boundaries which are favored nucleation sites for subgrain formation; the former are also more prone to grain fragmentation by GDRX (Geometric Dynamic Recrystallization) in the zones subjected to severe plastic deformation. These mechanisms would result in an enhanced fragmentation process in the Ti6242 that softened the latter compared to the work-hardened β grains of Ti17 rendering the Ti6242 more prone to plastic deformation and subsequent fragmentation-rotation. Eventually, the dominant development of BCC simple shear texture components observed in the thermomechanical affected zone of the weld joint is an additional argument that tends to confirm that the deformation process predominantly took place in the β domain.

In such severe thermo-mechanical processing conditions, β-titanium exhibits high recovery rates. Due to that fact, the increase in misorientation between the fragmented rotating sub-structures generally manifest slow kinetics that allegedly does not imply long-range motion of the crystalline interfaces. Nevertheless, the microstructural observations reported in Figure 9 and Figure 12 in the vicinity of the interfacial junction revealed that mutual β-grain boundary motions occurred across the interfacial junction between the β fragmenting grains belonging to the Ti17 and the Ti6242. This phenomenon led to a remarkable β microstructure continuity in the transition zone between the two alloys, regardless of the local alloying composition differences between the in-contact materials. As mentioned in [39], a recrystallization process is "the formation of new grain structures in a deformed material by the generation and the migration of high angle grain boundaries driven by the stored energy of deformation". Consequently, the previously described β-fragmentation process can be requalified as a recrystallization process. Recovery and recrystallization are competitive processes that are both driven by the stored energy of deformation. As a result, the interfacial migration mechanism was presumably mainly caused by differences in defect density and interfacial energy between the in-contact crystalline interfaces. The latter locally resulted in a driving force for the migration of the grain boundaries. This type of grain refinement process is often referred to as a Continuous Dynamic Recrystallization (CDRX) process in the literature [28], [40]. Therefore, such CDRX process led to the progressive transformation of the initial β boundaries, delimiting both contacting alloys as homophase crystalline interfaces [41], in favor of interfacial β grains by mutual grain boundary motion.

The local repartition of substitutional elements across the interfacial zone manifests clear evidence of a global interdiffusion phenomenon on an approximately 4 µm thick band along the transition zone. The latter probably mainly arose at high-temperature and under BCC crystal structure, when the interfacial zone became cohesive. The fitting of the element diffusion profiles (Figure 7) through Gaussian error-functions showed a slight shift of the center of the fitted error-function away from the WL towards Ti17. This slight shift can be explained based on the effects of the alloying elements on phase stability: Mo and Cr elements are strong β-stabilizers while Al element is an α-stabilizer [42]. Zr is known as a neutral element, but it was demonstrated to increase the β-stabilizing

effects (propensity to suppress the metastable α"/ ω phases in favor single β phase) when associated with other β-stabilizer elements in β-titanium alloys [43]. Sn is also considered as a neutral element, but it acts as an α stabilizer in the presence of other α stabilizers [42]. The amount of α-stabilizer elements was still large enough to facilitate the precipitation of the α' laths between the WL and the center of the fitted error-functions. The estimated diffusion coefficients deduced from the fitting of the experimental profiles with error-functions displayed an order of magnitude of 10^{-1} µms^{-1}. Such values are consistent with the order of magnitude of the β-titanium lattice diffusivity, which is around 10^{-1} µm^2.s^{-1} [44], [45] under the presumed interfacial temperature values reached during the steady-state rubbing process *id est* 1200°C. Contrary to measured diffusion values in similar solid-state assembling processes [46], no short-circuit diffusion features caused by large strains were noticed in the present configuration. The absence of observable dislocation-pipe assisted diffusion as described in [42] or [43] may be explained by the occurrence of continuous dynamic recrystallization in the junction zone. The balance between the dislocation generation and the rate of dislocation annihilation might have inhibited the assisted diffusion along short-circuiting paths because of the low resulting dislocation density inside the subgrain structures [49].

When the motion of the oscillating part stopped, the near interfacial zone between the alloys locally underwent a critical cooling. On the one hand, α' laths spanned across the parent refined β subgrains of the Ti6242 presenting a slab-like morphology in self-similarity pattern arrangements [50]. The textured aspect of the α' precipitates (see orientations data in Figure 4) is most likely due to the variants selections according to the BOR from the strong high-temperature β preferred orientation that developed during the hot deformation process. In principle, the phase transformation reaction for the α' phase precipitation should be partitionless and the α' laths should locally inherit the local chemical composition of the parent β phase. However, in practice, it is rarely possible to completely avoid diffusion phenomena. In the close interfacial zone, a strong partitioning between the α' and β phase was notably revealed. Indeed, a remarkable depletion in β stabilizing elements (Cr, Mo and arguably Zr) was observed within the precipitated α' plates, accompanied with thin pile-ups of the latter along the α'/β interfaces (Figure 8). The phenomenon is notably clearly perceptible on the chrome element

which is the strongest β stabilizer among the alloys components (Figure 8.b). This finding suggests that during the phase transformation, which operates throughout the progressive and coordinate collapse of the β crystal planes, an important portion of β stabilizer atoms crossed the migrating interphase boundary. The latter observation consequently indicates an element partitioning at the moving phase boundary probably controlled by a local equilibrium condition [51]. The low solubility of the Cr and Mo components in the HCP phase [52] presumably led to the diffusion of these elements towards the adjacent β-BCC phase upon phase transformation and consequently caused the continuous accumulation of these migrating elements in front of the α'/β interfaces. A local equilibrium condition at the moving phase boundary would push the local elements pile-ups forward the transformation front, which would finally result in the observed gradient-aspect pile-ups of rejected elements along the phase boundary. Besides, the local boundary conditions and notably the high concentration of misfit dislocations between the phase boundaries might have enhanced the transport phenomena by pipe-assisted diffusion. Similar element partitioning features were notably reported and are described in details by authors [53] in precipitation-hardened Mn-enriched TRIP-steel at the martensite/austenite phase boundaries. On the other hand, a full retention of the high temperature BCC β phase is detected at ambient temperature in the β-metastable alloy Ti17 forming the observed intermingled α'/β interfacial structures (Figures 9, 10 and 11).

Based on the previous results, the scenario presented in Figure 15 is proposed to describe the formation of the cohesive junction between the studied dissimilar alloys:

(Step I) Before friction, stable Ti_xO_y oxide layers of a few nanometers in width were initially present on the ground surfaces of the titanium alloy work-pieces. Similarly as in other solid-state joining processes, the disruption of those oxides is a prerequisite condition for successfully forming a metallic bond [10], [54]. During the friction process, the energy dissipation originating from the contact friction interactions was substantially transformed into thermal energy. The increase in temperature at the vicinity of the faying/reciprocating surfaces led to the thermal softening of the

materials. The plastic flow resulting from this softening might have enhanced the fragmentation, breaking up and/or dispersion of the oxide layers.

(Step II) The thermal energy arising from the irreversibility of such a frictional process caused the materials to be subjected to high-temperature values (higher than the β-transus temperature in both materials). The latter would favor a progressive closure of the voids between the faying surfaces by mutual plastic deformation. As well described by authors in diffusion bonding processes [5], [7], such local high-temperature conditions promote the fast dissociation of the titanium oxides at the oxide/metal interface ; followed by bulk-diffusion of the reaction products in the metallic solute matrix. The round-shapes porosities observed in Figure 5 may be explained by the incomplete mechanical closure of the interfacial voids. The latter might be formed by entrapped gaseous species resulting from the incomplete reduction reaction of the oxides.

(Step III – Step V) Such thermomechanical processing conditions led to a β-fragmentation process through a progressive reorganization of the geometrically necessary dislocations into low angle boundaries and then to high angle boundaries. Likewise other solid-state assembling processes, it was already shown by the authors in [55], [56], [57] that, in metal-to-metal contacts, fast surface atomic diffusion and surface relaxation are key factors yielding to the primal solid-state bonding between crystalline materials. When a sufficient adhesion occurred between the frictionning parts, a migration of the crystalline interfaces assisted by a continuous dynamic recrystallization process is demonstrated across the junction zone. The grain boundary migration kinetics were probably caused by differences in defect density and interfacial energy between the in-contact crystalline interfaces, ultimately leading to the formation of the cohesive junction depicted in Step V. Once the cohesive junction established, the thermal source is eventually mainly sustained by internal dissipative processes (*id est* by the degeneration of the plastic deformation energy in the form of thermal energy). The thermomechanical coupling under the imposed deformation conditions yields to the apparent self-regulated behavior of the process during the axial shortening phase.

(Step VI) Under high cooling rate, the composition differences between the alloys resulted in the formation of different detected phases in the transitional zone (α' martensitic laths in the Ti6242 side and room temperature single β-metastable phase in the Ti17 side). Intermingled grain-refined structures sharing both α' and β phase structures were observed in the interfacial zone.

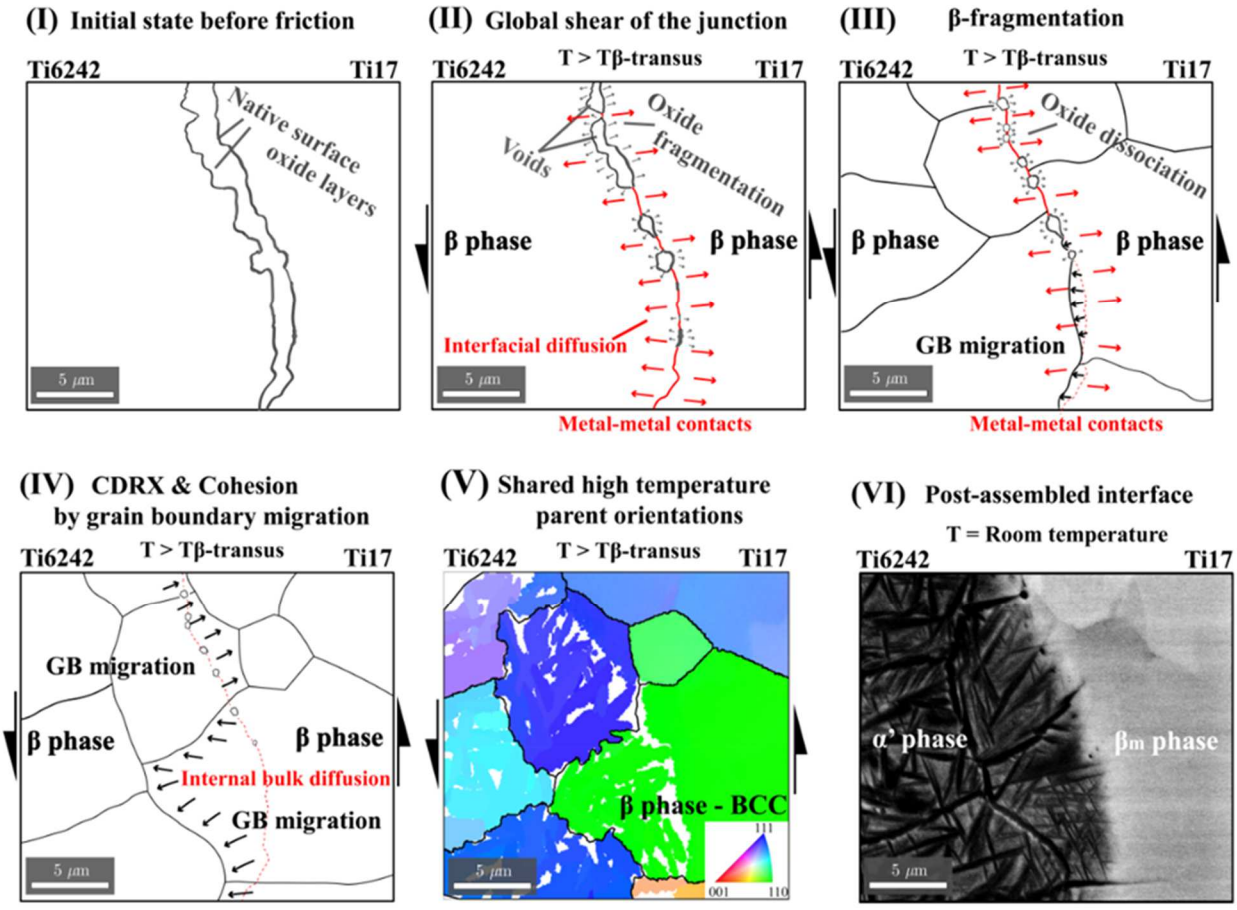

Figure 15: Schematic representation of the stages leading to interface bonding during LFW.

5 Conclusion

The interfacial features of linear friction welding between two dissimilar but mutually soluble titanium alloys (Ti17 and Ti6242) were examined. The thorough analysis of the interface and its surrounding allowed to identify the underlying microstructural mechanisms leading to the successful cohesion between the assembled work-pieces. Joining occurred in the single-phase β domain by the active migration of the crystalline interfaces from one grain to another across the junction zone assisted by a continuous dynamic recrystallization process. Besides, the motion of the interfacial grain

boundaries arose despite the chemical composition difference between the examined titanium alloys. It was shown that the resulting interfacial β grains present a common β-parent crystallographic orientation and an internal diffuse interface. Once the reciprocating motion stopped both materials experienced rapid cooling from the β domain. Under these β quenching conditions, the chemical composition heterogeneity across the diffuse interfaces caused a strong difference in local phase precipitation. It resulted in the formation of intermingled grains of HCP phase in the Ti6242-dominant side and of stabilized $\beta_{metastable}$ structure in Ti17-dominant side. It was shown that these intermingled structures perfectly verified the Burgers orientation relationship, which finally confirmed the common crystallographic origin of their high-temperature β parent grains.

6 Data Availability

The raw/processed data required to produce these findings cannot be shared at this time as it is part of an ongoing study.

7 Acknowledgement

The authors gratefully acknowledge the financial support of the French National Research Agency (ANR) through the OPTIMUM ANR-14-CE27-0017 project. The authors would also like to thank the Hauts-de-France Region and the European Regional Development Fund (ERDF) 2014/2020 for the co-funding of this work. The authors would also like to thank ACB for providing LFW samples as well as Airbus for their technical support

8 References

[1] J. L. Jellison, « The Role of Surface Contaminants in the Solid-State Welding of Metals », in *Treatise on Clean Surface Technology*, Boston, MA: Springer US, 1987, p. 205‑234.

[2] N. Bay, « Mechanisms producing metallic bonds in cold welding », *Welding research supplement*, p. 137‑142, mai-1983.

[3] H. A. Mohamed et J. Washburn, « Mechanism of Solid State Pressure Welding », *Weld. Res. Suppl.*, p. 9.

[4] Y. Saito, H. Utsunomiya, N. Tsuji, et T. Sakai, « Novel ultra-high straining process for bulk materials - Development of the accumulative roll-bonding (ARB) process », *Acta Mater*, vol. 47, n° 2, p. 579‑583, 1999.

[5] Z. A. Munir, « Analytical treatment of the role of surface oxide layers in the sintering of metals », *J. Mater. Sci.*, vol. 14, nº 11, p. 2733‑2740, nov. 1979.
[6] Y. Takahashi, K. Inoue, et K. Nishiguchi, « Identification of void shrinkage mechanisms », *Acta Metall. Mater.*, vol. 41, nº 11, p. 3077‑3084, nov. 1993.
[7] Y. Takahashi, T. Nakamura, et K. Nishiguchi, « Dissolution process of surface oxide film during diffusion bonding of metals », *J. Mater. Sci.*, vol. 27, nº 2, p. 485‑498, 1992.
[8] N. F. Kazakov, Éd., *Diffusion Bonding of materials*. Oxford: Oxford Scientific Press, 1985.
[9] M. Lagos et C. Retamal, « An alternate theoretical approach to solid-state bonding », *Scr. Mater.*, vol. 64, nº 5, p. 402‑405, mars 2011.
[10] A. A. Shirzadi, H. Assadi, et E. R. Wallach, « Interface evolution and bond strength when diffusion bonding materials with stable oxide films », *Surf. Interface Anal.*, vol. 31, nº 7, p. 609‑618, juill. 2001.
[11] J. Bos et H. Moes, « Frictional Heating of Tribological Contacts », *J. Tribol.*, vol. 117, nº 1, p. 171, janv. 1995.
[12] J. Romero, M. M. Attallah, M. Preuss, M. Karadge, et S. E. Bray, « Effect of the forging pressure on the microstructure and residual stress development in Ti–6Al–4V linear friction welds », *Acta Mater.*, vol. 57, nº 18, p. 5582‑5592, oct. 2009.
[13] Y. Ji, Z. Chai, D. Zhao, et S. Wu, « Linear friction welding of Ti–5Al–2Sn–2Zr–4Mo–4Cr alloy with dissimilar microstructure », *J. Mater. Process. Technol.*, vol. 214, nº 4, p. 979‑987, avr. 2014.
[14] Y. Guo, Y. Chiu, M. M. Attallah, H. Li, S. Bray, et P. Bowen, « Characterization of Dissimilar Linear Friction Welds of α-β Titanium Alloys », *J. Mater. Eng. Perform.*, vol. 21, nº 5, p. 770‑776, mai 2012.
[15] G. D. Wen, T. J. Ma, W. Y. Li, S. Q. Wang, H. Z. Guo, et D. L. Chen, « Strain-controlled fatigue properties of linear friction welded dissimilar joints between Ti–6Al–4V and Ti–6.5Al–3.5Mo–1.5Zr–0.3Si alloys », *Mater. Sci. Eng. A*, vol. 612, p. 80‑88, août 2014.
[16] P. Zhao et L. Fu, « Strain hardening behavior of linear friction welded joints between TC11 and TC17 dissimilar titanium alloys », *Mater. Sci. Eng. A*, vol. 621, p. 149‑156, janv. 2015.
[17] A. A. Ward, Y. Zhang, et Z. C. Cordero, « Junction growth in ultrasonic spot welding and ultrasonic additive manufacturing », *Acta Mater.*, vol. 158, p. 393‑406, 2018.
[18] L. X. Sun, M. Q. Li, et H. Li, « Interface characteristics and recrystallization mechanism of dissimilar titanium bonds », *J. Mater. Sci.*, vol. 53, nº 7, p. 5380‑5388, avr. 2018.
[19] F. Bachmann, R. Hielscher, et H. Schaeben, « Texture Analysis with MTEX – Free and Open Source Software Toolbox », *Solid State Phenom.*, vol. 160, p. 63‑68, févr. 2010.
[20] F. Bachmann, R. Hielscher, et H. Schaeben, « Grain detection from 2d and 3d EBSD data—Specification of the MTEX algorithm », *Ultramicroscopy*, vol. 111, nº 12, p. 1720‑1733, déc. 2011.
[21] D. Ballat-Durand, S. Bouvier, M. Risbet, et W. Pantleon, « Multi-scale and multi-technic microstructure analysis of a linear friction weld of the metastable-β titanium alloy Ti-5Al-2Sn-2Zr-4Mo-4Cr (Ti17) towards a new Post-Weld Heat Treatment », *Mater. Charact.*, vol. 144, p. 661‑670, oct. 2018.
[22] D. Ballat-Durand, S. Bouvier, M. Risbet, et W. Pantleon, « Through analysis of the microstructure changes during linear friction welding of the near-α titanium alloy Ti-6Al-2Sn-4Zr-2Mo (Ti6242) towards microstructure optimization », *Mater. Charact.*, vol. (Under peer-review).
[23] H. M. Otte, « Mechanism of the martensitic transformation in titanium and its alloys », in *The Science, Technology and Application of Titanium*, Elsevier, 1970, p. 645‑657.

[24] Banerjee S., Mukhopadhyay P., *Phase Transformations - Examples fromTitanium and Zirconium alloys*, vol. 12. Elsevier Science, 2007.
[25] L. Germain, S. R. Dey, M. Humbert, et N. Gey, « Determination of parent orientation maps in advanced titanium-based alloys », *J. Microsc.*, vol. 227, nº 3, p. 284‑291, sept. 2007.
[26] L. Germain, N. Gey, R. Mercier, P. Blaineau, et M. Humbert, « An advanced approach to reconstructing parent orientation maps in the case of approximate orientation relations: Application to steels », *Acta Mater.*, vol. 60, nº 11, p. 4551‑4562, juin 2012.
[27] W. G. Burgers, « On the process of transition of the cubic-body-centered modification into the hexagonal-close-packed modification of zirconium », *Physica*, vol. 1, nº 7‑12, p. 561‑586, mai 1934.
[28] S. Gourdet et F. Montheillet, « A model of continuous dynamic recrystallization », *Acta Mater.*, vol. 51, nº 9, p. 2685‑2699, mai 2003.
[29] J. Baczynski et J. J. Jonas, « Texture development during the torsion testing of α-iron and two IF steels », *Acta Materialia*, p. 4273‑4288, 1996.
[30] M. Karadge, M. Preuss, C. Lovell, P. J. Withers, et S. Bray, « Texture development in Ti–6Al–4V linear friction welds », *Mater. Sci. Eng. A*, vol. 459, nº 1‑2, p. 182‑191, juin 2007.
[31] E. Dalgaard, P. Wanjara, J. Gholipour, X. Cao, et J. J. Jonas, « Linear friction welding of a near-β titanium alloy », *Acta Mater.*, vol. 60, nº 2, p. 770‑780, janv. 2012.
[32] S. Li, I. J. Beyerlein, et M. A. M. Bourke, « Texture formation during equal channel angular extrusion of fcc and bcc materials: comparison with simple shear », *Mater. Sci. Eng. A*, vol. 394, nº 1‑2, p. 66‑77, mars 2005.
[33] G. Lütjering et J. C. Williams, *Titanium*, 2nd edition. Berlin; New York: Springer, 2003.
[34] T. Sakai, A. Belyakov, R. Kaibyshev, H. Miura, et J. J. Jonas, « Dynamic and post-dynamic recrystallization under hot, cold and severe plastic deformation conditions », *Prog. Mater. Sci.*, vol. 60, p. 130‑207, mars 2014.
[35] D. Kuhlmann-Wilsdorf et N. Hansen, « Geometrically necessary, incidental and subgrain boundaries », *Scr. Metall. Mater.*, vol. 25, nº 7, p. 1557‑1562, juill. 1991.
[36] W. Pantleon et N. Hansen, « Dislocation boundaries—the distribution function of disorientation angles », *Acta Mater.*, vol. 49, nº 8, p. 1479‑1493, mai 2001.
[37] R. Sedláček, W. Blum, J. Kratochvíl, et S. Forest, « Subgrain formation during deformation: Physical origin and consequences », *Metall. Mater. Trans. A*, vol. 33, nº 2, p. 319‑327, févr. 2002.
[38] D. Raabe, « Investigation of contribution of {123} slip planes to development of rolling textures in bcc metals by use of Taylor models », *Materials Science and Technology*, p. 455‑460, mai-1995.
[39] R. D. Doherty *et al.*, « Current issues in recrystallization: a review », *Mater. Sci. Eng. A*, p. 56, 1997.
[40] K. Huang et R. E. Logé, « A review of dynamic recrystallization phenomena in metallic materials », *Mater. Des.*, vol. 111, p. 548‑574, déc. 2016.
[41] A.P. Sutton et R. W. Balluffi, *Interfaces in crystalline materials*, Oxford University Press. 1995.
[42] S. (Srikumar) Banerjee et P. (Pradip) Mukhopadhyay, *Phase transformations : examples from titanium and zirconium alloys*. Elsevier, 2007.
[43] M. Abdel-Hady, H. Fuwa, K. Hinoshita, H. Kimura, Y. Shinzato, et M. Morinaga, « Phase stability change with Zr content in β-type Ti–Nb alloys », *Scr. Mater.*, nº 57, p. 1000‑1003, 2007.
[44] G. Neumann et C. Tuijn, *Self-diffusion and impurity diffusion in pure metals: Handbook of experimental data*. Amsterdam: Pergamon, 2009.

[45] H. Nakajima et M. Koiwa, « Diffusion in Titanium. », *ISIJ Int.*, vol. 31, nº 8, p. 757‑766, août 1991.
[46] I. E. Gunduz, T. Ando, E. Shattuck, P. Y. Wong, et C. C. Doumanidis, « Enhanced diffusion and phase transformations during ultrasonic welding of zinc and aluminum », *Scr. Mater.*, vol. 52, nº 9, p. 939‑943, mai 2005.
[47] A. L. Ruoff et R. W. Balluffi, « Strain-Enhanced Diffusion in Metals. II. Dislocation and Grain-Boundary Short-Circuiting Models », *J. Appl. Phys.*, vol. 34, nº 7, p. 1848‑1853, juill. 1963.
[48] A. L. Ruoff, « Enhanced Diffusion during Plastic Deformation by Mechanical Diffusion », *J. Appl. Phys.*, vol. 38, nº 10, p. 3999‑4003, sept. 1967.
[49] M. Cohen, « Self-diffusion during plastic deformation ». Commemorative lecture by the fifteenth gold medalist of the japan institute of metals.
[50] J. W. Elmer, T. A. Palmer, S. S. Babu, W. Zhang, et T. DebRoy, « Phase transformation dynamics during welding of Ti–6Al–4V », *J. Appl. Phys.*, vol. 95, nº 12, p. 8327‑8339, juin 2004.
[51] M. Hillert, *Phase Equilibria, Phase Diagrams and Phase Transformations*, Second edition. Cambridge university press, 2007.
[52] H. Nakajima, K. Ogasawara, S. Yamaguchi, et M. Koiwa, « Diffusion of Cromium in alpha titanium and its alloys », *Mater. Trans. JIM*, vol. 31, nº 4, p. 249‑254, 1990.
[53] O. Dmitrieva *et al.*, « Chemical gradients across phase boundaries between martensite and austenite in steel studied by atom probe tomography and simulation », *Acta Mater.*, vol. 59, nº 1, p. 364‑374, janv. 2011.
[54] S. Koyama, M. Takahashi, et K. Ikeuchi, « Behavior of Superficial Oxide Film at Solid-State Diffusion-Bonded Interface of Tin », *Mater. Trans.*, vol. 45, nº 2, p. 300‑302, 2004.
[55] Y. Lu, J. Y. Huang, C. Wang, S. Sun, et J. Lou, « Cold welding of ultrathin gold nanowires », *Nat. Nanotechnol.*, vol. 5, nº 3, p. 218‑224, mars 2010.
[56] T. Kizuka, K. Yamada, et N. Tanaka, « Time-resolved high-resolution electron microscopy of solid state direct bonding of gold and zinc oxide nanocrystallites at ambient temperature », *Appl. Phys. Lett.*, vol. 70, nº 8, p. 964‑966, févr. 1997.
[57] T. Kizuka, « Atomic Process of Point Contact in Gold Studied by Time-Resolved High-Resolution Transmission Electron Microscopy », *Phys. Rev. Lett.*, vol. 81, nº 20, p. 4448‑4451, nov. 1998.

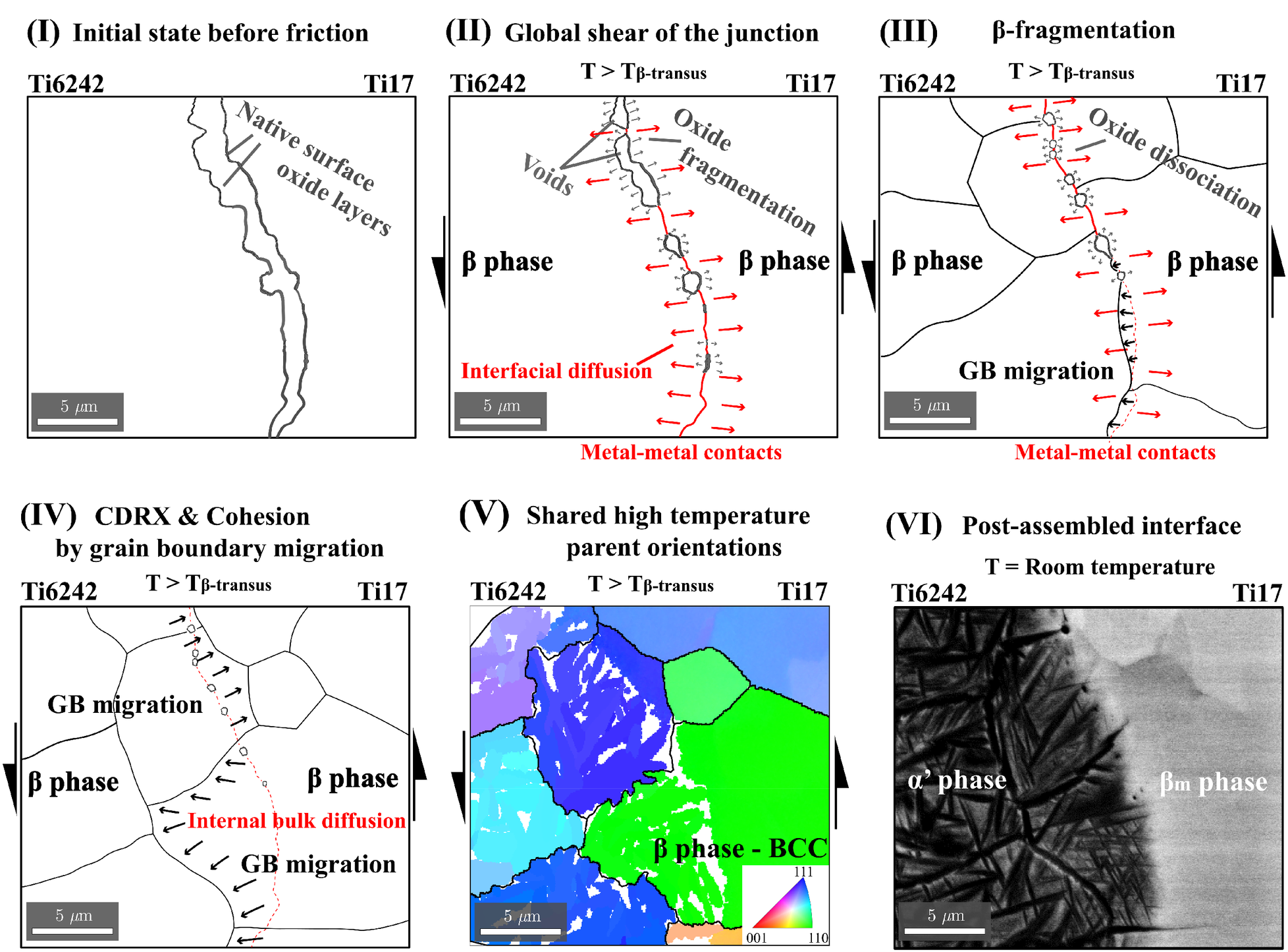
(I) Initial state before friction
Ti6242
Ti17
Native surface oxide layers
5 μm
(II) Global shear of the junction
T > Tβ-transus
Ti6242
Ti17
Oxide fragmentation
Voids
β phase
β phase
Interfacial diffusion
5 μm
Metal-metal contacts
(III) β-fragmentation
T > Tβ-transus
Ti6242
Ti17
Oxide dissociation
β phase
β phase
GB migration
5 μm
Metal-metal contacts
(IV) CDRX & Cohesion by grain boundary migration
T > Tβ-transus
Ti6242
Ti17
GB migration
β phase
β phase
Internal bulk diffusion
GB migration
5 μm
(V) Shared high temperature parent orientations
T > Tβ-transus
Ti6242
Ti17
β phase - BCC
111
001
110
5 μm
(VI) Post-assembled interface
T = Room temperature
Ti6242
Ti17
α' phase
βm phase
5 μm